

Revealing Superconducting Chiral Edge Modes via Resistance Distributions

Linghao Huang,^{1,2} Dongheng Qian,^{1,2} and Jing Wang^{1,2,3,4,*}

¹State Key Laboratory of Surface Physics and Department of Physics, Fudan University, Shanghai 200433, China

²Shanghai Research Center for Quantum Sciences, Shanghai 201315, China

³Institute for Nanoelectronic Devices and Quantum Computing, Fudan University, Shanghai 200433, China

⁴Hefei National Laboratory, Hefei 230088, China

Inducing superconducting correlations in quantum anomalous Hall (QAH) states offers a promising route to realize topological superconductivity with chiral Majorana edge modes. However, the definitive identification of these modes is challenging. Here we propose detecting superconducting chiral edge modes via the probability distribution of the resistance, or equivalently the charge transmission of QAH-superconductor heterojunctions. Remarkably, the distribution for coherent edge exhibits distinct characteristics for different topological superconducting phases in sufficiently long junctions, and this difference remains robust against weak decoherence. These findings provide new insights into transport phenomena beyond the clean limit and highlight the resistance distribution as a compelling signature for distinguishing topological superconducting phases.

The superconducting chiral edge modes, which are unidirectional and dissipationless Bogoliubov edge states, could emerge along the boundaries of a two-dimensional chiral topological superconductor (TSC) [1–10] and have potential applications in quantum information [11–16]. A promising approach to realizing these modes is to induce superconducting pair correlation in the chiral edge states of quantum Hall (QH) or quantum anomalous Hall (QAH) insulators via the proximity effect [17–29]. Distinctive transport phenomena have been observed in the QH-SC and QAH-SC junctions [24–28] due to the charge-neutral nature of these edge modes [30–51]. A significant goal is to achieve $p + ip$ TSC, which hosts a single chiral Majorana edge mode exhibiting quantized transport and interference signatures [34–37, 52]. However, its experimental confirmation remains elusive. At the same time, disorder and decoherence are inherent in realistic experimental devices [26, 28], making it essential to study transport signatures beyond the idealized clean limit. In particular, understanding the resistance distribution under these effects is vital [43, 48, 49], especially as such distributions can now be measured directly in experiments [26]. Theoretically, an intriguing question is whether these distributions reveal novel behaviors due to the presence of exotic Majorana edge states. Experimentally, it is crucial to determine whether the distribution, beyond just its mean value, provides stronger evidence to distinguish between different topological phases in SC.

In this Letter, we present a comprehensive analytical investigation of disorder-induced resistance distributions in QAH-SC junctions, supported by extensive numerical simulations. Using the transfer matrix formalism, we show that the quantum transport of edge modes under disorder can be intuitively described as random rotations on the Bloch sphere. This framework offers a more rigorous approach than that of [43], which relied on simplifications from renormalization group analysis. We specifically consider QAH-SC heterojunctions commonly implemented in experiments as illustrated in Fig. 1, where

the QAH insulator has a Chern number $C = 1$, hosting a single chiral electron edge mode [53–57], while the SC region is characterized by a Bogoliubov-de Gennes (BdG) Chern number $N = 1$ or $N = 2$, corresponding to transport mediated by one or two chiral Bogoliubov edge modes (CBEM), respectively. The key results are summarized in Table I, which outlines the probability distributions of charge transmission (defined in Eq. (1)) across different scenarios. Notably, for sufficiently long junctions, the distributions for $N = 1$ and $N = 2$ CBEM exhibit distinct characteristics. Moreover, these differences remain robust against decoherence, suggesting that resistance distributions serve as a compelling signature to distinguish between different topological phases of SC.

Edge transport with $N = 2$ CBEM. By stacking a normal SC onto the middle region of a $C = 1$ QAH insulator, one can experimentally implement a QAH-SC-QAH heterojunction in Fig. 1(a). We first consider the middle region of the heterojunction to be in the same topological phase as the $C = 1$ QAH state with broken charge $U(1)$ symmetry, namely a TSC with BdG Chern number

TABLE I. Summary of the probability distributions of charge transmission fraction T in two commonly implemented heterojunction configurations. $f(T)$: the probability density function of T . \mathcal{N} : normal distribution. χ^2 : chi-squared distribution. $U[-1, 1]$: uniform distribution over $[-1, 1]$.

Configuration	CBEM	Length	Cases	$f(T)$
QAH-SC-QAH	$N = 2$	short	(i)	\mathcal{N} or χ^2
		long	(ii)	$U[-1, 1]$
	$N = 1$		(iii)	\mathcal{N}
QAH-SC	$N = 2$	short	(i)	\mathcal{N} or χ^2
		long	(ii)	$U[-1, 1]$
	$N = 1$	short	(i)	\mathcal{N} or χ^2
		long	(iv)	generalized arcsine

$N = 2$, which would be the case when the SC proximity gap is smaller than the insulating QAH bulk gap [6, 37]. In Nambu basis $(c_k^\dagger, c_{-k})^T$, the effective edge Hamiltonian for TSC is described as $H_{\text{edge}} = vk\tau_0 - \mu\tau_z + \Delta\tau_x$, where v is the edge mode velocity, μ is the chemical potential, and $\Delta = \Delta_0k$ is the SC pairing amplitude. $\tau_{x,y,z}$ are Pauli matrices in Nambu space. Accordingly, the single chiral electron edge mode of the QAH state splits into a particle-hole conjugate pair of CBEM of the TSC state, also known as chiral Andreev edge modes [24]. In Fig. 1(a), normal transmission and Andreev transmission [58] refer to the processes where an electron from the QAH region enters the SC and exits as either an electron or a hole, with transmission coefficients denoted by T_{ee} and T_{eh} , respectively. We define the charge transmission fraction [59] from lead 2 to 3 as,

$$T \equiv T_{ee} - T_{eh}. \quad (1)$$

The presence of static disorder induces spatial variations in the potential and pairing amplitude experienced by the edge modes. This effect is effectively described by random fluctuations of the parameters (v, μ, Δ_0) in H_{edge} , making T a random variable governed by a probability distribution—this forms the central focus of our study. Experimentally, this distribution can be observed by varying the magnetic field or the electron density [26, 48, 60]. We divide the SC region into L segments labeled by the index $\ell = 1, 2, \dots, L$, where $L \propto \mathcal{L}/\xi_d$. Here \mathcal{L} denotes the junction length and ξ_d is the disorder correlation length. Within each segment, the parameters (v, μ, Δ_0) remain constant in the local Hamiltonian H_ℓ , as depicted in Fig. 1(b). The final state is obtained via the transfer matrix method [33, 61, 62]

$$\Psi_f = (\psi_e, \psi_h)^T = \mathbb{T}_L \cdots \mathbb{T}_2 \mathbb{T}_1 \Psi_i \equiv \mathbb{T} \Psi_i, \quad (2)$$

where $\Psi_i = (1, 0)^T$ is the incident state. The transfer matrix for the ℓ -th SC segment \mathbb{T}_ℓ is given by $\mathbb{T}_\ell = P_\ell^{-1} \Lambda_\ell P_\ell$, where Λ_ℓ represents the propagation matrix of the segment and P_ℓ transforms the Nambu basis into the eigenbasis of H_ℓ . \mathbb{T}_ℓ is intuitively interpreted as a rotation on the Bloch sphere, with a rotation angle α_ℓ around an axis \mathbf{n}_ℓ , as depicted in Fig. 1(c). Here we consider $L > 2\ell_d/a$, where ℓ_d is the decay length of CBEM wavefunction, and a is the lattice constant. Therefore, the crossed Andreev reflection and elastic co-tunneling processes are neglected [46, 63–65]. As detailed in [62], both α_ℓ and \mathbf{n}_ℓ exhibit small fluctuations, with standard deviations satisfying $\delta\alpha_\ell \ll 2\pi$ and $|\delta\mathbf{n}_\ell| \ll 1$. The cumulative effect of these random rotations can be approximated as a single rotation by an angle α around an axis $\mathbf{n} \equiv (n_x, n_y, n_z)$, such that $\mathbb{T} \propto e^{i\alpha(\mathbf{n}\cdot\boldsymbol{\sigma})/2}$, where $\boldsymbol{\sigma} = (\sigma_x, \sigma_y, \sigma_z)$ are Pauli matrices. The final state then takes the form $\Psi_f = (\cos(\alpha/2) + in_z \sin(\alpha/2), i(n_x + in_y) \sin(\alpha/2))^T$, and the charge transmission fraction is given by $T = |\psi_e|^2 - |\psi_h|^2 = n_z^2 + (1 - n_z^2) \cos \alpha$.

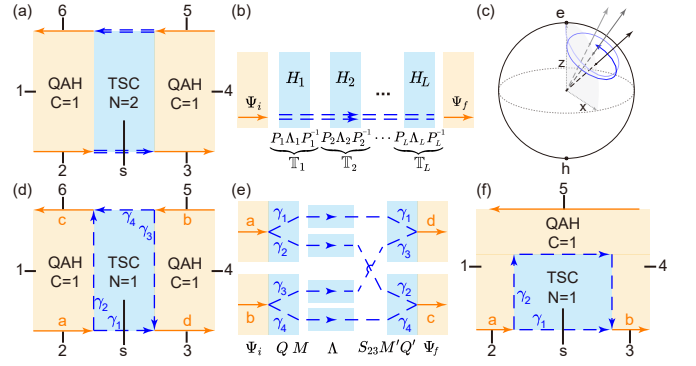


FIG. 1. (a) The QAH-SC-QAH junction with $N = 2$ CBEM. The orange and dashed blue arrows represent the chiral electron edge mode of QAH state and the CBEM of TSC state, respectively. (b) Transfer matrix construction for the junction shown in (a). (c) Evolution of the state on the Bloch sphere. Both the axis and rotation angle exhibit weak fluctuations. The north (south) pole on the Bloch sphere represents a pure electron (hole) state. (d,e) The QAH-SC-QAH junction with $N = 1$ CBEM, and the corresponding transfer matrix construction. (f) The QAH-SC junction with $N = 1$ CBEM.

The distribution of T exhibits distinct yet general behaviors depending on the length of SC region, as analyzed in the following cases.

Case (i): For a relatively short QAH-SC-QAH junction (small L as $2\ell_d/a < L < 10^2$) in Fig. 1(a), T approximately follows either a normal distribution (\mathcal{N}), or a chi-squared distribution (χ^2).

In this regime, fluctuations in the rotation axis are negligible, allowing us to approximate $\mathbf{n} \approx \bar{\mathbf{n}}_\ell$. As a result, the state undergoes sequential rotations around a nearly fixed axis, with each segment contributing a random rotation angle. The total rotation angle is $\alpha = \sum_{\ell=1}^L \alpha_\ell$. By the central limit theorem, after multiple segments, α follows a normal distribution with mean $\bar{\alpha} = L\bar{\alpha}_\ell$ and standard deviation $\delta\alpha = \sqrt{L}\delta\alpha_\ell$, irrespective of the specific distribution of the individual rotation angles α_ℓ . When L , and thus $\delta\alpha$, is small, we can expand α around $\bar{\alpha}$ up to second order: $\cos \alpha \approx \cos \bar{\alpha} - \sin \bar{\alpha} \Delta\alpha - \cos \bar{\alpha} (\Delta\alpha)^2/2$, where $\Delta\alpha$ follows a normal distribution. Therefore, T approximately follows a normal distribution when $\sin \bar{\alpha}$ is not close to zero, and a chi-squared distribution when $\sin \bar{\alpha} \approx 0$ [62]. As the junction length varies, the distribution of T oscillates between normal and chi-squared distributions. This behavior extends beyond the results in [48], where only a normal distribution was proposed.

Case (ii): For a long QAH-SC-QAH junction (large L as $L > 10^4$) in Fig. 1(a), T approximates a continuous uniform distribution over $[-1, 1]$, denoted as $U[-1, 1]$.

As L increases, the fluctuations of the rotation axis become significant, causing the state to spread across the entire Bloch sphere, as illustrated in Fig. 1(c). The ergodicity theorem [66] states that a point undergoing re-

peated rotations about two noncollinear axes eventually becomes uniformly distributed over the sphere. Since the fluctuating rotation axes in our system satisfy this condition, the final state Ψ_f becomes equidistributed on the Bloch sphere, leading to $T \sim U[-1, 1]$. A more rigorous derivation is provided in [62].

Edge transport with $N = 1$ CBEM. Next, we consider the case where the middle SC region of the heterojunction has a BdG Chern number $N = 1$, hosting a single self-conjugate CBEM, also known as chiral Majorana edge mode [6, 37]. As shown in Fig. 1(d), two incoherent incident charged modes, originating from different sources and labeled a and b , decompose into four Majorana edge modes, labeled γ_1 through γ_4 . Among them, γ_2 and γ_3 undergo braiding, after which all four modes recombine into two outgoing charged modes, labeled c and d . This process, depicted in Fig. 1(e), is described by

$$\Psi_f = Q' M' S_{23} \Lambda M Q \Psi_i. \quad (3)$$

Here, Ψ_i is a four-dimensional vector representing the initial state. The transformation sequence, proceeding from right to left, is as follows: Q accounts for propagation near the corners upon entering the SC region, M transforms the Nambu basis into the Majorana basis, Λ describes propagation within the SC region in the Majorana basis, S_{23} captures the braiding of γ_2 and γ_3 , M' rotates the Majorana basis back to the Nambu basis, and Q' describes propagation near the corners before exiting the SC region. The matrix Λ is diagonal, with random phase factors reflecting the well-separated and decoupled nature of the Majorana modes away from the SC region's corners. However, near these corners, the Majorana modes overlap, leading to non-trivial coupling. This coupling takes the form $\eta \tau_z$ in the Nambu basis, where η is a disorder-dependent coupling coefficient [40, 43]. This coupling term corresponds to the chemical potential term in H_{edge} . Consequently, the effect of random coupling is captured by $Q = \text{diag}(\mathbb{T}^a, \mathbb{T}^b)$ and $Q' = \text{diag}(\mathbb{T}^c, \mathbb{T}^d)$, where \mathbb{T}^ζ represents the total transfer matrix at corner $\zeta = a, b, c, d$, structured similarly to the transfer matrix product in Eq. (2).

Case (iii): For the QAH-SC-QAH junction with $N = 1$ CBEM shown in Fig. 1(d), T consistently follows a normal distribution, regardless of the junction length.

The normal distribution of T stems from two key factors. First, the incoherent nature of the incident electrons ensures that the phase factors in Λ do not affect T , making it independent of the junction length. Second, coupling occurs only near the corners, leading to a small effective L when computing \mathbb{T}^ζ . As a result, each \mathbb{T}^ζ can be treated as a random rotation around a fixed axis, analogous to Case (i). A detailed derivation of this result is provided in [62].

Then we examine an alternative junction configuration [24–28], depicted in Fig. 1(f). This setup, known as a QAH-SC junction, is realized by stacking a normal SC

onto the edge region of a $C = 1$ QAH insulator. When the SC region has a BdG Chern number $N = 2$, the charge transmission fraction T from lead 2 to 3 in QAH-SC junction matches that of the QAH-SC-QAH junction in Fig. 1(a). Therefore, we focus on the SC region has $N = 1$. In this configuration, the incident charged mode a splits into two Majorana modes, γ_1 and γ_2 , within the SC region, which subsequently recombine and emerge as the outgoing charged mode b . A key distinction between this setup and the QAH-SC-QAH junction in Fig. 1(d) is that in the QAH-SC junction, the Majorana modes originate from the same source, preserving their coherence. This coherence leads to different transport behaviors of T , depending on the junction length. Specifically, the final state can be expressed as

$$\Psi_f = \mathbb{T}^b M' \Lambda M \mathbb{T}^a \Psi_i. \quad (4)$$

Here, fluctuations near the corners are negligible compared to those along the edges of the SC region. This allows us to approximate the total transfer matrix as $\bar{\mathbb{T}}^{-1} M' \Lambda M \bar{\mathbb{T}}$, where $\bar{\mathbb{T}}$ represents the average transfer matrix at the corner. As a result, the entire process can be interpreted as a random rotation by an angle α around a fixed axis \mathbf{n} , with α and \mathbf{n} determined by Λ and $M \bar{\mathbb{T}}$, respectively. For small L , the fluctuation of α remains small, making the system behave similarly to Case (i). However, as L increases, the system exhibits qualitatively different behavior.

Case (iv): For a long QAH-SC junction (large L as $L > 10^4$) with $N = 1$ CBEM in Fig. 1(f), T approximately follows a generalized arcsine distribution.

As discussed in Case (i), $\delta\alpha \propto \sqrt{L}$, which becomes significant for large L . Therefore, $\cos \alpha$ will converge to the standard arcsine distribution [67], then T obeys a shifted and rescaled variant of the standard arcsine distribution, with the probability density function

$$f(T) = \begin{cases} \frac{1}{\pi \sqrt{(1-A)^2 - (T-A)^2}}, & (T \in [1-2A, 1]) \\ 0, & (T \notin [1-2A, 1]) \end{cases} \quad (5)$$

where $A = n_z^2$. This distribution is characterized by a U-shaped profile that peaks at the maximal value 1 and the minimal value $(1 - 2A)$ of T .

Finally, when the SC region of the junction is topologically trivial ($N = 0$), two CBEM emerge along the interface between the SC and QAH. Therefore, the edge mode transport characteristics closely resemble those of the $N = 2$ case [62].

Numerical calculations. To validate the analytical results presented above, we numerically compute T in each case. We implemented two-dimensional tight-binding Hamiltonians of both QAH and SC for the configurations in Fig. 1 (a,d,f) on a rectangular geometry. The disorder is introduced through a uniformly distributed onsite potential with $\xi_d = a \equiv 1$. The charge transmission T is then calculated using the recursive Green's

function method [68–73]. Additional numerical details are provided in [62].

The results for the junction configuration of Fig. 1(a) are presented in Fig. 2. Here, \bar{T} denotes the mean charge transmission fraction from lead 2 to 3. When disorder is introduced into the SC region, \bar{T} exhibits oscillations with a decaying amplitude as the junction length L increases, eventually converging to zero. Meanwhile, the fluctuations in T increase, as shown in Fig. 2(a,b). For $L \gtrsim 2\ell_d$, T follows a normal or chi-squared distribution, as illustrated in Fig. 2(c) and Fig. 2(d), respectively, in accordance with Case (i). For sufficiently large L , such that $L \gtrsim 10^4$, the distribution of T approaches a continuous uniform distribution $U[-1, 1]$, as shown in Fig. 2(e), corresponding to Case (ii).

For the junction configuration of Fig. 1(d), the results are presented in Fig. 3(a,b). When $L \gtrsim 2\ell_d$, both the mean and fluctuations of T remain constant as L varies, with \bar{T} aligning with its value in the clean limit. Furthermore, the distribution of T follows a normal distribution, consistent with Case (iii), confirming that this distribution arises from the random coupling of Majorana modes near the junction corners. Next, the results for the QAH-SC junction of Fig. 1(f) are shown in Fig. 3(c,d). While \bar{T} exhibits oscillations with decaying amplitude—similar

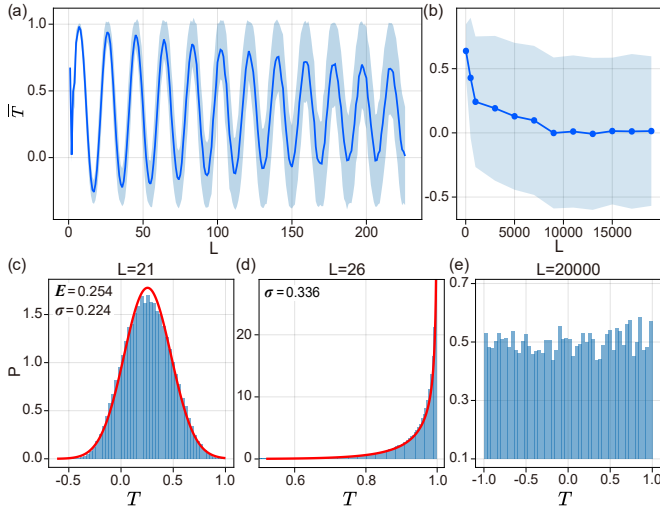


FIG. 2. Mean and distribution of the charge transmission fraction T for the junction in Fig. 1(a). (a,b) T vs L , where solid lines and shaded region indicate the mean and standard deviation, respectively. (c-e) The distributions of T for different L , with histograms representing numerical results and red lines showing fitted distributions. (c) The distribution is fitted with a normal distribution $f(T) = \frac{1}{\sigma\sqrt{2\pi}} e^{-\frac{(T-E)^2}{2\sigma^2}}$. (d) The distribution is fitted with a chi-squared distribution $f(T) = \frac{1}{\sigma\sqrt{\pi(1-T)}} e^{-\frac{1-T}{\sigma^2}}$. (e) The mean and standard deviation of T are 8.54×10^{-3} and 0.582, respectively, which match those of a uniform distribution $U[-1, 1]$.

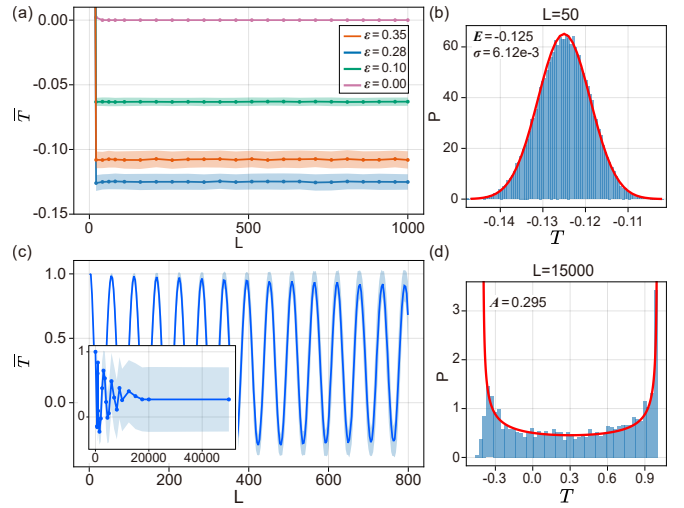


FIG. 3. (a,b) Numerical results of T for junction in Fig. 1(d). (a) \bar{T} vs L , where ε denotes the incident electron energy. The solid lines and shading indicate the mean and standard deviation, respectively. (b) Distribution of T for $\varepsilon = 0.28$, which follows a normal distribution depicted as red line. (c,d) Numerical results for junction of Fig. 1(f). (c) \bar{T} vs L . (d) Distribution of T , with the red line showing the fitting distribution as a generalized arcsine distribution in Eq. (5).

to the $N = 2$ case—it does not necessarily converge to zero, depending on the incident electron energy ε . Furthermore, for sufficiently large L , such that $L \gtrsim 10^4$, the distribution transitions to a generalized arcsine form, as predicted in Case (iv). The left peak is broadened due to the neglected fluctuations of the rotation axis in the analytical analysis, which introduce slight variations in the lower bound of the distribution.

Decoherence. Two additional factors, loss and decoherence, play a significant role in shaping experimental observations beyond the effects of disorder [26]. Loss occurs when particles tunnel into magnetic vortices and escape through the vortex line to the substrate [46, 48, 74]. This process reduces the norm of Ψ_f , thus compressing the distribution of T without altering its overall shape. Decoherence, on the other hand, results from inelastic scattering with other gapless degrees of freedom, which can be induced by magnetic vortices, ineffective SC proximity, or thermal fluctuations [49]. When the decoherence effect is weak, the effect of decoherence can be conceptualized as the edge mode that has a probability p of undergoing a single inelastic scattering event during its propagation. The resulting effective charge transmission fraction for different scenarios in Fig. 1(a,d,f) is shown in Fig. 4, where the distribution for $N = 2$ CBEM remains distinct from that for $N = 1$ CBEM, indicating that the characteristic behavior of the distribution in the coherent process persists under sufficiently weak decoherence. As the decoherence effect intensifies, characterized by an

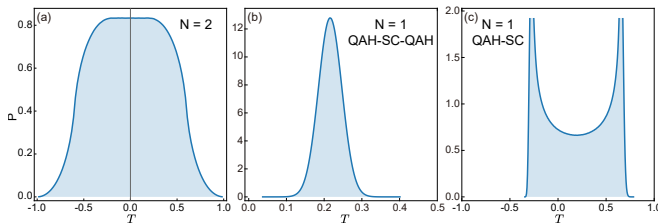


FIG. 4. (a,b,c) Decoherence effect in scenarios Fig. 1(a,d,f), respectively. The distribution is calculated from Monte Carlo sampling [62], and we set $p = 0.4$. We set the distribution of T without decoherence follows $U[-1, 1]$, $\mathcal{N}(0.3, 0.05^2)$ and arcsin distribution with $A = 0.6$ for Fig. 1(a,d,f), respectively.

increase in p and the occurrence of multiple scattering events, the distribution for the scenario in Fig. 1(a) will become logarithmic divergent peaked at $T = 0$, while the scenarios in Fig. 1(d,f) become bell-shaped peaked at finite T [62].

Discussions. The experimentally measurable resistances are determined by T . Taking QAH-SC junction shown in Fig. 1(f) as an example. The current is from lead 1 to the grounded SC, namely $I_1 = -I_s = I$, and voltage leads are on electrodes 2, 3, 4, and 5. The downstream resistance [19, 25, 28] is given by the generalized Landauer-Büttiker formula [75]

$$R_d \equiv R_{3s} = \frac{V_3 - V_s}{I} = \frac{h}{e^2} \frac{T}{1 - T}, \quad (6)$$

where h is the Planck constant, e is the electrical charge. Thus, T can be directly extracted from the measured R_d . Other nonlocal resistances in different scenarios are provided in [62].

Our theory shows that the probability distribution of charge transmission T provides a signature distinguish between the different topological phases of the SC region. As summarized in Table I, for sufficiently long junctions, the distributions for $N = 1$ and $N = 2$ CBEM exhibit distinct characteristics. Moreover, these differences remain robust against weak decoherence. Given the stark differences between these distributions, they provide stronger evidence for phase differentiation, offering extra insight than mean alone, which may be insufficient to distinguish between topological phases of SC region [28].

Acknowledgment. We thank Yuanbo Zhang for enlightening discussions. This work is supported by the Natural Science Foundation of China through Grants No. 12350404 and No. 12174066, the Innovation Program for Quantum Science and Technology through Grant No. 2021ZD0302600, the Science and Technology Commission of Shanghai Municipality under Grants No. 23JC1400600, No. 24LZ1400100 and No. 2019SHZDZX01.

* wjingphys@fudan.edu.cn

- [1] G. Moore and N. Read, Nonabelions in the fractional quantum hall effect, *Nucl. Phys. B* **360**, 362 (1991).
- [2] N. Read and D. Green, Paired states of fermions in two dimensions with breaking of parity and time-reversal symmetries and the fractional quantum hall effect, *Phys. Rev. B* **61**, 10267 (2000).
- [3] A. Kitaev, Anyons in an exactly solved model and beyond, *Ann. Phys.* **321**, 2 (2006).
- [4] L. Fu and C. L. Kane, Superconducting proximity effect and majorana fermions at the surface of a topological insulator, *Phys. Rev. Lett.* **100**, 096407 (2008).
- [5] F. Wilczek, Majorana returns, *Nat. Phys.* **5**, 614 (2009).
- [6] X.-L. Qi, T. L. Hughes, and S.-C. Zhang, Chiral topological superconductor from the quantum hall state, *Phys. Rev. B* **82**, 184516 (2010).
- [7] J. D. Sau, R. M. Lutchyn, S. Tewari, and S. Das Sarma, Generic new platform for topological quantum computation using semiconductor heterostructures, *Phys. Rev. Lett.* **104**, 040502 (2010).
- [8] J. Alicea, Majorana fermions in a tunable semiconductor device, *Phys. Rev. B* **81**, 125318 (2010).
- [9] X.-L. Qi and S.-C. Zhang, Topological insulators and superconductors, *Rev. Mod. Phys.* **83**, 1057 (2011).
- [10] S. R. Elliott and M. Franz, Colloquium: Majorana fermions in nuclear, particle, and solid-state physics, *Rev. Mod. Phys.* **87**, 137 (2015).
- [11] C. Nayak, S. H. Simon, A. Stern, M. Freedman, and S. Das Sarma, Non-abelian anyons and topological quantum computation, *Rev. Mod. Phys.* **80**, 1083 (2008).
- [12] R. S. K. Mong, D. J. Clarke, J. Alicea, N. H. Lindner, P. Fendley, C. Nayak, Y. Oreg, A. Stern, E. Berg, K. Shtengel, and M. P. A. Fisher, Universal topological quantum computation from a superconductor-abelian quantum hall heterostructure, *Phys. Rev. X* **4**, 011036 (2014).
- [13] D. J. Clarke, J. Alicea, and K. Shtengel, Exotic circuit elements from zero-modes in hybrid superconductor-quantum-hall systems, *Nat. Phys.* **10**, 877 (2014).
- [14] B. Lian, X.-Q. Sun, A. Vaezi, X.-L. Qi, and S.-C. Zhang, Topological quantum computation based on chiral majorana fermions, *Proc. Natl. Acad. Sci. U.S.A.* **115**, 10938 (2018).
- [15] Y. Hu and C. L. Kane, Fibonacci topological superconductor, *Phys. Rev. Lett.* **120**, 066801 (2018).
- [16] C. W. J. Beenakker, P. Baireuther, Y. Herasymenko, I. Adagideli, L. Wang, and A. R. Akhmerov, Deterministic creation and braiding of chiral edge vortices, *Phys. Rev. Lett.* **122**, 146803 (2019).
- [17] Z. Wan, A. Kazakov, M. J. Manfra, L. N. Pfeiffer, K. W. West, and L. P. Rokhinson, Induced superconductivity in high-mobility two-dimensional electron gas in gallium arsenide heterostructures, *Nat. Commun.* **6**, 7426 (2015).
- [18] F. Amet, C. T. Ke, I. V. Borzenets, J. Wang, K. Watanabe, T. Taniguchi, R. S. Deacon, M. Yamamoto, Y. Bomze, S. Tarucha, and G. Finkelstein, Supercurrent in the quantum hall regime, *Science* **352**, 966 (2016).
- [19] G.-H. Lee, K.-F. Huang, D. K. Efetov, D. S. Wei, S. Hart, T. Taniguchi, K. Watanabe, A. Yacoby, and P. Kim, Inducing superconducting correlation in quantum hall edge states, *Nat. Phys.* **13**, 693 (2017).
- [20] M. R. Sahu, X. Liu, A. K. Paul, S. Das, P. Raychaudhuri,

- J. K. Jain, and A. Das, Inter-landau-level andreev reflection at the dirac point in a graphene quantum hall state coupled to a nbse₂ superconductor, *Phys. Rev. Lett.* **121**, 086809 (2018).
- [21] S. Matsuo, K. Ueda, S. Baba, H. Kamata, M. Tateno, J. Shabani, C. J. Palmström, and S. Tarucha, Equal-spin andreev reflection on junctions of spin-resolved quantum hall bulk state and spin-singlet superconductor, *Sci. Rep.* **8**, 3454 (2018).
- [22] A. Seredinski, A. W. Draelos, E. G. Arnault, M.-T. Wei, H. Li, T. Fleming, K. Watanabe, T. Taniguchi, F. Amet, and G. Finkelstein, Quantum hall-based superconducting interference device, *Sci. Adv.* **5**, eaaw8693 (2019).
- [23] H. Vignaud, D. Perconte, W. Yang, B. Kousar, E. Wagner, F. Gay, K. Watanabe, T. Taniguchi, H. Courtois, Z. Han, H. Sellier, and B. Sacépé, Evidence for chiral supercurrent in quantum hall josephson junctions, *Nature* **624**, 545 (2023).
- [24] L. Zhao, E. G. Arnault, A. Bondarev, A. Seredinski, T. F. Q. Larson, A. W. Draelos, H. Li, K. Watanabe, T. Taniguchi, F. Amet, H. U. Baranger, and G. Finkelstein, Interference of chiral andreev edge states, *Nature Phys.* **16**, 862 (2020).
- [25] Ö. Gül, Y. Ronen, S. Y. Lee, H. Shapourian, J. Zauberman, Y. H. Lee, K. Watanabe, T. Taniguchi, A. Vishwanath, A. Yacoby, and P. Kim, Andreev reflection in the fractional quantum hall state, *Phys. Rev. X* **12**, 021057 (2022).
- [26] L. Zhao, Z. Iftikhar, T. F. Q. Larson, E. G. Arnault, K. Watanabe, T. Taniguchi, F. Amet, and G. Finkelstein, Loss and decoherence at the quantum hall-superconductor interface, *Phys. Rev. Lett.* **131**, 176604 (2023).
- [27] M. Hatefipour, J. J. Cuozzo, J. Kanter, W. M. Strickland, C. R. Allemang, T.-M. Lu, E. Rossi, and J. Shabani, Induced superconducting pairing in integer quantum hall edge states, *Nano Lett.* **22**, 6173 (2022).
- [28] A. Uday, G. Lippertz, K. Moors, H. F. Legg, R. Joris, A. Bliesener, L. M. C. Pereira, A. A. Taskin, and Y. Ando, Induced superconducting correlations in a quantum anomalous hall insulator, *Nat. Phys.* **20**, 1589 (2024).
- [29] Y. Sato, S. Nagahama, I. Belopolski, R. Yoshimi, M. Kawamura, A. Tsukazaki, N. Kanazawa, K. S. Takahashi, M. Kawasaki, and Y. Tokura, Molecular beam epitaxy of superconducting FeSe_xTe_{1-x} thin films interfaced with magnetic topological insulators, *Phys. Rev. Mater.* **8**, L041801 (2024).
- [30] H. Hoppe, U. Zülicke, and G. Schön, Andreev reflection in strong magnetic fields, *Phys. Rev. Lett.* **84**, 1804 (2000).
- [31] F. Giazotto, M. Governale, U. Zülicke, and F. Beltram, Andreev reflection and cyclotron motion at superconductor—normal-metal interfaces, *Phys. Rev. B* **72**, 054518 (2005).
- [32] A. R. Akhmerov and C. W. J. Beenakker, Detection of valley polarization in graphene by a superconducting contact, *Phys. Rev. Lett.* **98**, 157003 (2007).
- [33] J. A. M. van Ostaay, A. R. Akhmerov, and C. W. J. Beenakker, Spin-triplet supercurrent carried by quantum hall edge states through a josephson junction, *Phys. Rev. B* **83**, 195441 (2011).
- [34] L. Fu and C. L. Kane, Probing neutral majorana fermion edge modes with charge transport, *Phys. Rev. Lett.* **102**, 216403 (2009).
- [35] A. R. Akhmerov, J. Nilsson, and C. W. J. Beenakker, Electrically detected interferometry of majorana fermions in a topological insulator, *Phys. Rev. Lett.* **102**, 216404 (2009).
- [36] S. B. Chung, X.-L. Qi, J. Maciejko, and S.-C. Zhang, Conductance and noise signatures of majorana backscattering, *Phys. Rev. B* **83**, 100512 (2011).
- [37] J. Wang, Q. Zhou, B. Lian, and S.-C. Zhang, Chiral topological superconductor and half-integer conductance plateau from quantum anomalous hall plateau transition, *Phys. Rev. B* **92**, 064520 (2015).
- [38] G. Strübi, W. Belzig, M.-S. Choi, and C. Bruder, Interferometric and noise signatures of majorana fermion edge states in transport experiments, *Phys. Rev. Lett.* **107**, 136403 (2011).
- [39] B. Lian, J. Wang, and S.-C. Zhang, Edge-state-induced andreev oscillation in quantum anomalous hall insulator-superconductor junctions, *Phys. Rev. B* **93**, 161401 (2016).
- [40] B. Lian, J. Wang, X.-Q. Sun, A. Vaezi, and S.-C. Zhang, Quantum phase transition of chiral majorana fermions in the presence of disorder, *Phys. Rev. B* **97**, 125408 (2018).
- [41] J. Wang and B. Lian, Multiple chiral majorana fermion modes and quantum transport, *Phys. Rev. Lett.* **121**, 256801 (2018).
- [42] M. Beconcini, M. Polini, and F. Taddei, Nonlocal superconducting correlations in graphene in the quantum hall regime, *Phys. Rev. B* **97**, 201403 (2018).
- [43] B. Lian and J. Wang, Distribution of conductances in chiral topological superconductor junctions, *Phys. Rev. B* **99**, 041404 (2019).
- [44] J. J. He, T. Liang, Y. Tanaka, and N. Nagaosa, Platform of chiral majorana edge modes and its quantum transport phenomena, *Commun. Phys.* **2**, 149 (2019).
- [45] A. Manesco, I. M. Flór, C.-X. Liu, and A. Akhmerov, Mechanisms of andreev reflection in quantum hall graphene, *SciPost Phys. Core* **5**, 045 (2022).
- [46] Y. Tang, C. Knapp, and J. Alicea, Vortex-enabled andreev processes in quantum hall-superconductor hybrids, *Phys. Rev. B* **106**, 245411 (2022).
- [47] N. Schiller, B. A. Katzir, A. Stern, E. Berg, N. H. Lindner, and Y. Oreg, Superconductivity and fermionic dissipation in quantum hall edges, *Phys. Rev. B* **107**, L161105 (2023).
- [48] V. D. Kurilovich, Z. M. Raines, and L. I. Glazman, Disorder-enabled andreev reflection of a quantum hall edge, *Nat. Commun* **14**, 2237 (2023).
- [49] Y. Hu, J. Wang, and B. Lian, Resistance distribution of decoherent quantum hall-superconductor edges (2024), [arXiv:2405.17550 \[cond-mat\]](https://arxiv.org/abs/2405.17550).
- [50] A. Nava, R. Egger, F. Hassler, and D. Giuliano, Non-abelian anyon statistics through ac conductance of a majorana interferometer, *Phys. Rev. Lett.* **133**, 146604 (2024).
- [51] A. Bondarev, G. Zhang, and H. U. Baranger, Transparent graphene-superconductor interfaces: Quantum hall and zero field regimes (2025), [arXiv:2502.13307 \[cond-mat.mes-hall\]](https://arxiv.org/abs/2502.13307).
- [52] L. Katayama, A. P. Schnyder, Y. Asano, and S. Ikegaya, Noise-to-current ratio divergence as a fingerprint of dispersing majorana edge modes (2025), [arXiv:2502.20921 \[cond-mat\]](https://arxiv.org/abs/2502.20921).
- [53] C.-Z. Chang, J. Zhang, X. Feng, J. Shen, Z. Zhang,

- M. Guo, K. Li, Y. Ou, P. Wei, L.-L. Wang, Z.-Q. Ji, Y. Feng, S. Ji, X. Chen, J. Jia, X. Dai, Z. Fang, S.-C. Zhang, K. He, Y. Wang, L. Lu, X.-C. Ma, and Q.-K. Xue, Experimental observation of the quantum anomalous hall effect in a magnetic topological insulator, *Science* **340**, 167 (2013).
- [54] J. G. Checkelsky, R. Yoshimi, A. Tsukazaki, K. S. Takahashi, Y. Kozuka, J. Falson, M. Kawasaki, and Y. Tokura, Trajectory of the anomalous hall effect towards the quantized state in a ferromagnetic topological insulator, *Nat. Phys.* **10**, 731 (2014).
- [55] X. Kou, S.-T. Guo, Y. Fan, L. Pan, M. Lang, Y. Jiang, Q. Shao, T. Nie, K. Murata, J. Tang, Y. Wang, L. He, T.-K. Lee, W.-L. Lee, and K. L. Wang, Scale-invariant quantum anomalous hall effect in magnetic topological insulators beyond the two-dimensional limit, *Phys. Rev. Lett.* **113**, 137201 (2014).
- [56] M. Mogi, R. Yoshimi, A. Tsukazaki, K. Yasuda, Y. Kozuka, K. S. Takahashi, M. Kawasaki, and Y. Tokura, Magnetic modulation doping in topological insulators toward higher-temperature quantum anomalous hall effect, *Appl. Phys. Lett.* **107**, 182401 (2015).
- [57] Y. Deng, Y. Yu, M. Z. Shi, Z. Guo, Z. Xu, J. Wang, X. H. Chen, and Y. Zhang, Quantum anomalous hall effect in intrinsic magnetic topological insulator MnBi_2Te_4 , *Science* **367**, 895 (2020).
- [58] A. Andreev *et al.*, Thermal conductivity of the intermediate state of superconductors ii, *Sov. Phys. JETP* **20**, 1490 (1965).
- [59] G. E. Blonder, M. Tinkham, and T. M. Klapwijk, Transition from metallic to tunneling regimes in superconducting microconstrictions: Excess current, charge imbalance, and supercurrent conversion, *Phys. Rev. B* **25**, 4515 (1982).
- [60] P. A. Lee, A. D. Stone, and H. Fukuyama, Universal conductance fluctuations in metals: Effects of finite temperature, interactions, and magnetic field, *Phys. Rev. B* **35**, 1039 (1987).
- [61] J.-X. Zhang and C.-X. Liu, Disordered quantum transport in quantum anomalous hall insulator-superconductor junctions, *Phys. Rev. B* **102**, 144513 (2020).
- [62] See Supplemental Material for more details, which cludes refs. [76–82].
- [63] T. H. Galambos, F. Ronetti, B. Hetényi, D. Loss, and J. Klinovaja, Crossed andreev reflection in spin-polarized chiral edge states due to the meissner effect, *Phys. Rev. B* **106**, 075410 (2022).
- [64] V. D. Kurilovich and L. I. Glazman, Criticality in the crossed andreev reflection of a quantum hall edge, *Phys. Rev. X* **13**, 031027 (2023).
- [65] N. Schiller, B. A. Katzir, A. Stern, E. Berg, N. H. Lindner, and Y. Oreg, Superconductivity and fermionic dissipation in quantum hall edges, *Phys. Rev. B* **107**, L161105 (2023).
- [66] V. I. Arnold and A. L. Krylov, Uniform distribution of points on a sphere and some ergodic properties of solutions of linear ordinary differential equations in a complex region, *Collected Works: Representations of Functions, Celestial Mechanics and KAM Theory, 1957–1965*, 413 (2009).
- [67] W. Feller, *An introduction to probability theory and its applications, Volume 2*, Vol. 81 (John Wiley & Sons, 1991).
- [68] D. J. Thouless and S. Kirkpatrick, Conductivity of the disordered linear chain, *J. Phys. C: Solid State Phys.* **14**, 235 (1981).
- [69] M. P. L. Sancho, J. M. L. Sancho, and J. Rubio, Quick iterative scheme for the calculation of transfer matrices: Application to mo (100), *J. Phys. F: Met. Phys.* **14**, 1205 (1984).
- [70] M. P. L. Sancho, J. M. L. Sancho, J. M. L. Sancho, and J. Rubio, Highly convergent schemes for the calculation of bulk and surface green functions, *J. Phys. F: Met. Phys.* **15**, 851 (1985).
- [71] A. MacKinnon, The calculation of transport properties and density of states of disordered solids, *Z. Physik B: Condens. Matter* **59**, 385 (1985).
- [72] S. Datta, *Lessons from Nanoelectronics: A New Perspective on Transport*, second edition ed., Lessons from Nanoscience: A Lecture Notes Series No. vol. 5 (World Scientific, New Jersey, 2017).
- [73] Q.-f. Sun and X. C. Xie, Quantum transport through a graphene nanoribbon–superconductor junction, *J. Phys.: Condens. Matter* **21**, 344204 (2009).
- [74] A. B. Michelsen, P. Recher, B. Braunecker, and T. L. Schmidt, Supercurrent-enabled andreev reflection in a chiral quantum hall edge state, *Phys. Rev. Research* **5**, 013066 (2023).
- [75] O. Entin-Wohlman, Y. Imry, and A. Aharony, Conductance of superconducting-normal hybrid structures, *Phys. Rev. B* **78**, 224510 (2008).
- [76] M. P. A. Fisher, Cooper-pair tunneling into a quantum hall fluid, *Phys. Rev. B* **49**, 14550 (1994).
- [77] B. Béri, J. N. Kupferschmidt, C. W. J. Beenakker, and P. W. Brouwer, Quantum limit of the triplet proximity effect in half-metal–superconductor junctions, *Phys. Rev. B* **79**, 024517 (2009).
- [78] K. V. Mardia and P. E. Jupp, eds., *Directional Statistics*, Wiley Series in Probability and Statistics (J. Wiley, Chichester New York, 2010).
- [79] Y. Kawada and K. Itô, On the probability distribution on a compact group. i, *Proceedings of the Physico-Mathematical Society of Japan. 3rd Series* **22**, 977 (1940).
- [80] M. Buttiker, Symmetry of electrical conduction, *IBM J. Res. Dev.* **32**, 317 (1988).
- [81] G. Cui, X. Yu, S. Iommelli, and L. Kong, Exact distribution for the product of two correlated gaussian random variables, *IEEE Signal Process. Lett.* **23**, 1662 (2016).
- [82] D. Zhang, M. Shi, T. Zhu, D. Xing, H. Zhang, and J. Wang, Topological axion states in the magnetic insulator MnBi_2Te_4 with the quantized magnetoelectric effect, *Phys. Rev. Lett.* **122**, 206401 (2019).

Supplementary Materials for “Revealing Superconducting Chiral Edge Modes via Resistance Distributions”

Linghao Huang,^{1,2} Dongheng Qian,^{1,2} and Jing Wang^{1,2,3,4,*}

¹*State Key Laboratory of Surface Physics and Department of Physics, Fudan University, Shanghai 200433, China*

²*Shanghai Research Center for Quantum Sciences, Shanghai 201315, China*

³*Institute for Nanoelectronic Devices and Quantum Computing, Fudan University, Shanghai 200433, China*

⁴*Hefei National Laboratory, Hefei 230088, China*

CONTENTS

I. Edge Mode Scattering in QAH-TSC Heterojunctions	2
II. Nonlocal Resistances and Generalized Landauer-Büttiker Formula	3
III. Derivation of Probability Distribution of Transmission Fraction	4
IV. Decoherence Effect and Particle Loss	7
A. Decoherence	7
B. Particle loss	10
V. Technical Details of Numerical Calculations	10
VI. Numerical Results	10
A. Numerical results for QAH-SC-QAH junction	10
B. Numerical results for QAH-SC junction	12
C. Numerical results for $N = 0$ cases	14
References	15

* wjingphys@fudan.edu.cn

I. EDGE MODE SCATTERING IN QAH-TSC HETEROJUNCTIONS

This section details the derivation of edge mode scattering in quantum anomalous Hall insulator (QAH)-chiral topological superconductor (TSC) heterojunctions, where QAH is in the Chern number $C = 1$ state and TSC is in the Bogoliubov-de Gennes (BdG) Chern number $N = 2$ state. An electron from the QAH region enters the TSC region, and subsequently another QAH region. Following Refs. [1, 2], we employ the transfer matrix method.

We solve the eigenvalue equation $H(x)\Psi(x) = \varepsilon\Psi(x)$, where ε is the incident electron energy. In the Nambu basis $(\psi(x), \psi^\dagger(x))^T$, the effective Hamiltonian is $H(x) = v(x)k\tau_0 - \mu(x)\tau_z + \Delta(x)k\tau_x$, where $k \equiv -i\partial_x$, $\tau_{x,y,z}$ are Pauli matrices and τ_0 is the identity matrix. We define the operator:

$$J(x) = \frac{\partial H}{\partial k} = \begin{pmatrix} v(x) & \Delta(x) \\ \Delta(x) & v(x) \end{pmatrix}, \quad (S1)$$

where $\Delta(x) = 0$ ($\neq 0$) in the QAH (TSC) region, and its square-root operator:

$$J^{\frac{1}{2}}(x) = \begin{pmatrix} c_0(x) & c_x(x) \\ c_x(x) & c_0(x) \end{pmatrix}, \quad c_{0,x}(x) = \frac{\sqrt{v(x) + \Delta(x)} \pm \sqrt{v(x) - \Delta(x)}}{2}, \quad (S2)$$

which satisfies $(J^{\frac{1}{2}}(x))^2 = J(x)$. Denoting $J^{-\frac{1}{2}}(x) = (J^{\frac{1}{2}}(x))^{-1}$, the TSC effective edge Hamiltonian can be diagonalized as:

$$\tilde{H}(x) = J^{-\frac{1}{2}}(x)H(x)J^{-\frac{1}{2}}(x) = \begin{pmatrix} k & \\ & k \end{pmatrix} - \frac{1}{\sqrt{[v(x)]^2 - [\Delta(x)]^2}} \begin{pmatrix} \mu(x) & \\ & -\mu(x) \end{pmatrix}, \quad (S3)$$

Transforming the eigenvalue equation as $\tilde{H}(x)\tilde{\Psi}(x) = \varepsilon\tilde{\Psi}(x)$ with $\tilde{\Psi}(x) = J^{\frac{1}{2}}(x)\Psi(x)$. Now the eigenvalue equation can be straightforwardly solved out:

$$\Psi_f/\Psi_i = \tilde{\Psi}_f/\tilde{\Psi}_i = e^{\int_{x_i}^{x_f} A(x)dx}, \quad A(x) = i \left[\varepsilon J^{-1}(x) + \frac{1}{[v(x)]^2 - [\mu(x)]^2} \begin{pmatrix} \mu(x) & \\ & -\mu(x) \end{pmatrix} \right], \quad (S4)$$

where $x_{i(f)}$ is the initial (final) position of the TSC region, and $\Psi_f = \Psi(x_f)$ is the final state, $\Psi_i = \Psi(x_i) = (1, 0)^T$ is the incident state. The presence of disorder in the TSC region makes the parameters $v(x)$, $\mu(x)$, $\Delta(x)$ fluctuate, rendering the integral in Eq. (S4) analytically intractable. For simplicity, we divide the TSC region into multiple segments, within each of which the parameters are independent of x , while the values of these parameters are randomly assigned between different segments. Then the integral in Eq. (S4) is transformed into a sum, thus the final state is:

$$\Psi_f = e^{A_L} \dots e^{A_2} e^{A_1} \Psi_i = P_L^{-1} \Lambda_L P_L \dots P_1^{-1} \Lambda_1 P_1 \Psi_i, \quad (S5)$$

where L denotes the total number of segment. In the second equality, the A_ℓ matrices are diagonalized piecewise. Denoting the transfer matrix $\mathbb{T}_\ell = P_\ell^{-1} \Lambda_\ell P_\ell$, we obtain the first line of Eq. (2) in the main text.

The explicit expressions for P_ℓ and Λ_ℓ are:

$$P_\ell = \begin{pmatrix} \frac{\sqrt{(v_\ell^2 - \Delta_\ell^2)\mu_\ell^2 + \Delta_\ell^2\varepsilon^2} - \mu_\ell\sqrt{v_\ell^2 - \Delta_\ell^2}}{\sqrt{\Delta_\ell^2\varepsilon^2 + (\sqrt{(v_\ell^2 - \Delta_\ell^2)\mu_\ell^2 + \Delta_\ell^2\varepsilon^2} - \mu_\ell\sqrt{v_\ell^2 - \Delta_\ell^2})^2}} & -\frac{\sqrt{(v_\ell^2 - \Delta_\ell^2)\mu_\ell^2 + \Delta_\ell^2\varepsilon^2} + \mu_\ell\sqrt{v_\ell^2 - \Delta_\ell^2}}{\sqrt{\Delta_\ell^2\varepsilon^2 + (\sqrt{(v_\ell^2 - \Delta_\ell^2)\mu_\ell^2 + \Delta_\ell^2\varepsilon^2} + \mu_\ell\sqrt{v_\ell^2 - \Delta_\ell^2})^2}} \\ \frac{\Delta_\ell\varepsilon}{\sqrt{\Delta_\ell^2\varepsilon^2 + (\sqrt{(v_\ell^2 - \Delta_\ell^2)\mu_\ell^2 + \Delta_\ell^2\varepsilon^2} - \mu_\ell\sqrt{v_\ell^2 - \Delta_\ell^2})^2}} & \frac{\Delta_\ell\varepsilon}{\sqrt{\Delta_\ell^2\varepsilon^2 + (\sqrt{(v_\ell^2 - \Delta_\ell^2)\mu_\ell^2 + \Delta_\ell^2\varepsilon^2} + \mu_\ell\sqrt{v_\ell^2 - \Delta_\ell^2})^2}} \end{pmatrix}, \quad (S6)$$

$$\Lambda_\ell = \begin{pmatrix} e^{\frac{i v_\ell \varepsilon - \sqrt{(v_\ell^2 - \Delta_\ell^2)\mu_\ell^2 + \Delta_\ell^2\varepsilon^2}}{v_\ell^2 - \Delta_\ell^2} L_\ell} & 0 \\ 0 & e^{\frac{i v_\ell \varepsilon + \sqrt{(v_\ell^2 - \Delta_\ell^2)\mu_\ell^2 + \Delta_\ell^2\varepsilon^2}}{v_\ell^2 - \Delta_\ell^2} L_\ell} \end{pmatrix},$$

where L_ℓ is the length of the ℓ -th TSC section.

Applying a gauge transformation to make ψ_e real, the wavefunction can be parameterized as $(\cos \theta/2, e^{i\phi} \sin \theta/2)^T$, where θ and ϕ are the polar and azimuthal angles on the Bloch sphere, respectively. Thus Ψ_i is on the north pole. As a 2×2 unitary matrix, \mathbb{T}_ℓ can be viewed as a rotation operator: $\mathbb{T}_\ell = N_\ell e^{\frac{i\alpha_\ell(\mathbf{n}_\ell \cdot \boldsymbol{\sigma})}{2}}$. From Eq. (S6), we find

$$N_\ell = e^{\frac{iL_\ell v_\ell \varepsilon}{v_\ell^2 - \Delta_\ell^2}}, \quad \alpha_\ell = \frac{2L_\ell \sqrt{(v_\ell^2 - \Delta_\ell^2)\mu_\ell^2 + \Delta_\ell^2\varepsilon^2}}{v_\ell^2 - \Delta_\ell^2} \text{ mod } 2\pi, \quad (S7)$$

$$\mathbf{n}_\ell = \left(\left[1 + \frac{\mu_\ell^2}{\varepsilon^2} \left(\frac{v_\ell^2}{\Delta_\ell^2} - 1 \right) \right]^{-\frac{1}{2}}, 0, \left[1 + \left[\frac{\mu_\ell^2}{\varepsilon^2} \left(\frac{v_\ell^2}{\Delta_\ell^2} - 1 \right) \right]^{-1} \right]^{-\frac{1}{2}} \right)^T.$$

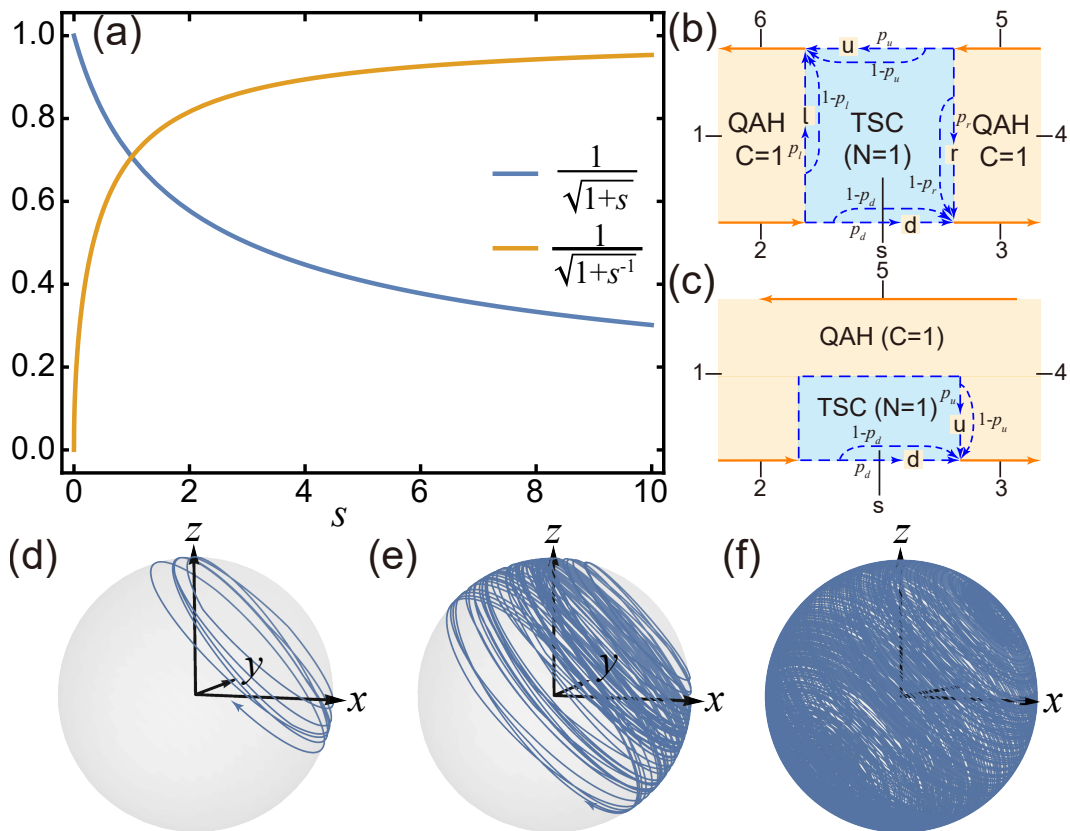


FIG. S1. (a) The x (blue line) and z (orange line) components of \mathbf{n}_ℓ . Here $s = \frac{\mu_\ell^2}{\varepsilon_\ell^2} \left(\frac{v_\ell^2}{\Delta_\ell^2} - 1 \right)$. Since $v_\ell > \Delta_\ell$, s is always positive. (b) Schematic diagrams for QAH-TSC-QAH junction. There are 7 leads (1-6 and s) attached to the junction, and four floating leads (l , r , u and d) shown at the boundaries of the TSC region. p_l and $1 - p_l$ are the probability of the edge modes entering and not entering the floating lead l , respectively, with similar meanings for p_r , p_u , and p_d . (c) Schematic diagrams for QAH-TSC junction. There are 6 leads attached to the junction, and two floating leads (u and d) at the boundaries of the TSC region. (d)-(f) The evolution of the state, where the parameters are: $\varepsilon = 1$, $L_\ell = 1$, μ_ℓ is uniformly distributed over 0.45 to 0.55 ($U[0.45, 0.55]$), $v_\ell \sim U[0.95, 1.05]$, $\Delta_\ell \sim U[0.45, 0.55]$, and L is 20, 200, 2000 for (d), (e), (f), respectively.

The rotational axis always lies in the xoz plane, and the x and z components of \mathbf{n}_ℓ are plotted in Fig. S1(a). When the parameters in effective Hamiltonian fluctuate slightly due to disorder, \mathbf{n}_ℓ changes only slightly around a certain direction, especially when $s = \frac{\mu_\ell^2}{\varepsilon_\ell^2} \left(\frac{v_\ell^2}{\Delta_\ell^2} - 1 \right)$ is large. Therefore, the total transport process can be interpreted as the evolution of a point at north-pole under multiple rotation operations, as shown in Figs. S1(d-f). As shown in the figures, when L is small [Fig. S1(d)], the trajectory can be approximately described as the path of a point rotating around a fixed axis. As L grows, the region of motion for the point gradually disperses [Fig. S1(e)] until it covers the entire spherical surface [Fig. S1(f)].

Although the overall rotational outcome is complex, there exist two simple limits: (i) When $\varepsilon \rightarrow 0$, $s \rightarrow \infty$, \mathbf{n}_ℓ will fix at the z axis. Since the initial state is at the north pole, the final state will always be at the north pole, resulting in no Andreev conversion, and T is always 1. This can be attributed to the Pauli exclusion principle when forming the Cooper pair [1–4]. (ii) When $v_\ell \rightarrow \Delta_\ell$, $s \rightarrow 0$, \mathbf{n}_ℓ will fix at the x axis. The final state will lie on the a meridian great circle, the resulting T is randomly distributed over the interval $[-1, 1]$.

II. NONLOCAL RESISTANCES AND GENERALIZED LANDAUER-BÜTTIKER FORMULA

The nonlocal resistances measured in the QAH-SC heterojunction can be calculated using the generalized Landauer-Büttiker formula [5]. In the configuration of the QAH-SC-QAH junction shown in Fig. 1(a) of the main text, when

leads 2 to 6 are voltage probes, the multi-terminal formula is:

$$\begin{aligned}
I_1 &= \frac{e^2}{h}(V_1 - V_6), & I_2 &= \frac{e^2}{h}(V_2 - V_1), & I_3 &= \frac{e^2}{h}[(V_3 - V_s) + T_d(V_s - V_2) + R_d(V_s - V_5)] \\
I_4 &= \frac{e^2}{h}(V_4 - V_3), & I_5 &= \frac{e^2}{h}(V_5 - V_4), & I_6 &= \frac{e^2}{h}[(V_6 - V_s) + T_u(V_s - V_5) + R_u(V_s - V_2)] \\
I_2 &= I_3 = I_5 = I_6 = 0, & I_1 + I_2 + I_3 + I_4 + I_5 + I_6 + I_s &= 0,
\end{aligned} \tag{S8}$$

where $T_u = T_{u,ee} - T_{u,eh}$ is the charge transmission fraction from lead 5 to 6, $T_d = T_{d,ee} - T_{d,eh}$ is that from lead 2 to 3, $R_u = R_{u,ee} - R_{u,eh}$ is that from lead 2 to 6, and $R_d = R_{d,ee} - R_{d,eh}$ is that from lead 5 to 3. When the SC is in the $N = 2$ phase, $R_u = R_d = 0$ due to the absence of edge modes along the interface between QAH and SC. Solving the equations with respect to applied currents yields the quantized values of resistances measured on various leads. For example, if $I_s = 0$, then $I_1 = -I_4 = I$, the non-local resistances are (in units of h/e^2):

$$\begin{aligned}
R_{14} &= \frac{V_1 - V_4}{I} = \frac{2 - (R_d + R_u + T_d + T_u)}{(R_d - 1)(R_u - 1) - T_d T_u}, & R_{23} &= \frac{V_2 - V_3}{I} = -\frac{R_d R_u - (T_d - 1)(T_u - 1)}{(R_d - 1)(R_u - 1) - T_d T_u}, \\
R_{56} &= \frac{V_5 - V_6}{I} = \frac{R_d R_u - (T_d - 1)(T_u - 1)}{(R_d - 1)(R_u - 1) - T_d T_u}, & R_{2s} &= \frac{V_2 - V_s}{I} = \frac{1 - (R_d + T_u)}{(R_d - 1)(R_u - 1) - T_d T_u}, \\
R_{s3} &= \frac{V_s - V_3}{I} = -1 + \frac{1 - (R_u + T_d)}{(R_d - 1)(R_u - 1) - T_d T_u}, & \dots &
\end{aligned} \tag{S9}$$

When the junction is symmetric such that $T_u = T_d = T$, $R_u = R_d = R$, the above expressions can be simplified as:

$$R_{14} = \frac{2}{1 + T - R}, \quad R_{23} = \frac{1 + R - T}{1 + T - R}, \quad R_{56} = \frac{1 + R - T}{R - T - 1}, \quad R_{2s} = \frac{1}{1 + T - R}, \quad R_{s3} = \frac{R - T}{1 + T - R}, \quad \dots \tag{S10}$$

If SC is grounded $V_s = 0$ and $I_4 = 0$, then $I_1 = -I_s = I$, the non-local resistances are:

$$\begin{aligned}
R_{4s} &= \frac{V_4 - V_s}{I} = \frac{T_d}{(R_d - 1)(R_u - 1) - T_d T_u}, & R_{23} &= \frac{V_2 - V_3}{I} = \frac{1 - (R_d + T_d)}{(R_d - 1)(R_u - 1) - T_d T_u}, \\
R_{56} &= \frac{V_5 - V_6}{I} = \frac{R_u(1 - R_d) + T_d(1 - T_u)}{(R_d - 1)(R_u - 1) - T_d T_u}, & R_{s3} &= \frac{V_s - V_3}{I} = -\frac{T_d}{(R_d - 1)(R_u - 1) - T_d T_u}, \\
R_{2s} &= \frac{V_2 - V_s}{I} = \frac{1 - R_d}{(R_d - 1)(R_u - 1) - T_d T_u}, & \dots &
\end{aligned} \tag{S11}$$

And when $T_u = T_d = T$, $R_u = R_d = R$, the above expressions can be simplified as:

$$R_{4s} = \frac{T}{(R - 1)^2 - T^2}, \quad R_{23} = \frac{1}{1 + T - R}, \quad R_{56} = \frac{T - R}{1 + T - R}, \quad R_{s3} = \frac{T}{T^2 - (R - 1)^2}, \quad R_{2s} = \frac{1 - R}{(R - 1)^2 - T^2}, \quad \dots \tag{S12}$$

We point out that although the main text focuses on the behavior of T , the behavior of R is similar, because both of them are governed by the edge modes transports.

In the configuration of the QAH-SC junction shown in the shown in Fig. 1(f) of the main text, there is no reflection process due to the chiral nature of edge modes. The multi-terminal formula is:

$$\begin{aligned}
I_1 &= \frac{e^2}{h}(V_1 - V_5), & I_2 &= \frac{e^2}{h}(V_2 - V_1), & I_3 &= \frac{e^2}{h}[(V_3 - V_s) + T(V_s - V_2)] \\
I_4 &= \frac{e^2}{h}(V_4 - V_3), & I_5 &= \frac{e^2}{h}(V_5 - V_4), & I_2 &= I_3 = I_5 = 0, & I_1 + I_2 + I_3 + I_4 + I_5 + I_s &= 0.
\end{aligned} \tag{S13}$$

where $T = T_{ee} - T_{eh}$ is the charge transmission fraction from lead 2 to 3. If $V_s = 0$ while $I_4 = 0$, then $I_1 = -I_s = I$, the non-local resistances are:

$$R_{4s} = \frac{V_4 - V_s}{I} = \frac{T}{1 - T}, \quad R_{2s} = \frac{V_2 - V_s}{I} = \frac{1}{1 - T}, \quad R_{s3} = \frac{V_s - V_3}{I} = \frac{T}{T - 1}, \quad \dots \tag{S14}$$

III. DERIVATION OF PROBABILITY DISTRIBUTION OF TRANSMISSION FRACTION

This section derives the probability distribution of transmission fraction discussed in the main text. As shown in the previous section, $\mathbb{T}_\ell = P_\ell^{-1} \Lambda_\ell P_\ell = N_\ell e^{\frac{i\alpha_\ell(\mathbf{n}_\ell \cdot \boldsymbol{\sigma})}{2}}$ can be viewed as a rotation operator with rotational angle α_ℓ and rotational axis \mathbf{n}_ℓ . We use this property to prove the conclusions in the main text.

Case (i): \mathbf{n}_ℓ is fixed, and the number of sections L is small.

In this case, all P_ℓ s become the same, denoted as P_1 , then $\Psi_f = P_1^{-1}\Lambda_L P_1 \cdots P_1^{-1}\Lambda_1 P_1 \Psi_i = P_1^{-1}\Lambda_L \cdots \Lambda_1 P_1 \Psi_i$. As illustrated in the main text, the total effect of these rotation operations can be described as a total rotation with angle α around the axis \mathbf{n} :

$$\Psi_f = \mathbb{T}\Psi_i \propto e^{\frac{i\alpha(\mathbf{n}\cdot\sigma)}{2}} \Psi_i = \begin{pmatrix} \cos(\alpha/2) + in_z \sin(\alpha/2) \\ i(n_x + in_y) \sin(\alpha/2) \end{pmatrix}. \quad (\text{S15})$$

Since Λ_ℓ s are diagonal, the total rotational angle is just the sum of α_ℓ s: $\alpha = \sum_{\ell=1}^L \alpha_\ell$. Since the fluctuations of α_ℓ and L are small, α has a small fluctuation. To avoid other effects such as crossed Andreev reflection and elastic cotunneling [6–9], which will complicate the Andreev reflection process on which we focus, we assume that the smallest L is at least of order 10 ($> 2\ell_d/a$). According to the central limit theorem, the distribution of α approximately follows a normal distribution: $\alpha \sim N(L\bar{\alpha}_\ell, L\sigma_\ell^2)$, where $\bar{\alpha}_\ell$ and σ_ℓ^2 are the mean value and variance of α_ℓ .

The normal, Andreev, and charge transmission probabilities are the norms of the first and second components of Ψ_f , and their difference, respectively:

$$\begin{aligned} T_{ee} &= \frac{1}{2}(1 + n_z^2) + \frac{1}{2}(1 - n_z^2) \cos \alpha, \\ T_{eh} &= 1 - T_{ee} = \frac{1}{2}(1 - n_z^2) - \frac{1}{2}(1 - n_z^2) \cos \alpha, \\ T &= T_{ee} - T_{eh} = n_z^2 + (1 - n_z^2) \cos \alpha. \end{aligned} \quad (\text{S16})$$

Given the cosine term in the above equation, $T(\alpha) = T(\alpha')$, where $\alpha' = \alpha \bmod 2\pi$. The normal distribution of α results in a wrapped normal distribution [10] of α' , whose probability density function is:

$$f_w(\alpha') = \frac{1}{\sqrt{2\pi}\sigma} \sum_{k=-\infty}^{+\infty} \exp\left[-\frac{(\alpha' - \bar{\alpha}' - 2\pi k)^2}{2\sigma^2}\right], \quad (\text{S17})$$

where $\bar{\alpha}' = L\bar{\alpha}_i \bmod 2\pi$, $\sigma = \sqrt{L}\sigma_i$. According to Eq. (S16), T_{ee} , T_{eh} , and T are all of the form $A + (1 - A) \cos \alpha'$, thus their probability density function can be written as:

$$f(T) = \begin{cases} \frac{f_w(\arccos(\frac{T-A}{1-A})) + f_w(-\arccos(\frac{T-A}{1-A}))}{(1-A)\sqrt{1-(\frac{T-A}{1-A})^2}}, & T \in [1 - 2A, 1] \\ 0, & \text{otherwise} \end{cases}. \quad (\text{S18})$$

Since σ_i and L are small, only one k in Eq. (S17) gives a dominant contribution, making the distribution of α' approximately $f_w(\alpha') \sim N(\bar{\alpha}', \sigma^2)$. When $\bar{\alpha}'$ is not close to 0 or π , expanding α' around $\bar{\alpha}'$ to the first order: $\cos \alpha' \approx \cos \bar{\alpha}' - \sin \bar{\alpha}' \delta \alpha'$, then $T \approx A + (1 - A) \cos \bar{\alpha}' - (1 - A) \sin \bar{\alpha}' \delta \alpha'$, where $\delta \alpha' \sim N(0, \sigma^2)$, thus Eq. (S18) approximately becomes:

$$f(T) \approx \frac{1}{\sqrt{2\pi}\sigma_T} e^{-\frac{(T-E)^2}{2\sigma_T^2}}, \quad (\text{S19})$$

where $\sigma_T = (1 - A)\sigma \sin \bar{\alpha}'$, $E = A + (1 - A) \cos \bar{\alpha}'$. Therefore, T follows the normal distribution $N(E, \sigma_T^2)$. When $\bar{\alpha}' \approx 0$ or π , the first-order coefficient vanishes, we need to expand α' to the second order: $\cos \alpha' \approx \pm 1 \mp (\delta \alpha')^2/2$. $X = (\delta \alpha')^2$ follow a non-central $k = 1$ chi-squared distributed random variable, whose probability density function is: $f(X) = e^{-\frac{X}{2\sigma^2}} / (\sigma\sqrt{2\pi X})$, thus the probability density function of $T \approx A + (1 - A)(\pm 1 \mp X/2)$ is:

$$f(T) = \begin{cases} \frac{1}{\sqrt{\pi(1-T)\sigma_T}} e^{-\frac{1-T}{\sigma_T^2}}, & \bar{\alpha}' = 0 \\ \frac{1}{\sqrt{\pi(T-(2A-1))\sigma_T}} e^{-\frac{T-(2A-1)}{\sigma_T^2}}, & \bar{\alpha}' = \pi \end{cases}, \quad (\text{S20})$$

where $\sigma_T = \sqrt{1 - A}\sigma$. This means T follows a chi-squared distribution. In general, the distributions of T oscillate between normal and chi-squared distributions as L varies.

Case (ii): \mathbf{n}_ℓ fluctuates around a certain axis.

The theorem mentioned in the main text provides a simplified explanation of the uniform distribution of transmission. A more rigorous proof uses the theorem by Itô and Kawada [11]: Consider a stochastic process on a group G :

$S_L = R_1 R_2 \cdots R_L$, where R_i s are independent random variables distributed according to a single probability measure μ on G . The probability measure of S_L , denoted as μ^L , is the convolution power L of μ . If μ is an aperiodic probability measure, then the sequence μ^L converges in distribution to the normalized Haar measure on G .

Here we focus on group $G = SU(2)$. The fluctuation region of \mathbf{n}_ℓ defines the probability measure μ , whose support is not contained in a coset of a proper closed subgroup of G , thus it is aperiodic. The operation of a series of rotations constitutes a stochastic process on G . From the above theorem, after enough rotations, the probability measure will converge to the normalized Haar measure of $SU(2)$, meaning that Ψ_f is equidistributed on the Bloch sphere. Thus the z component of $\Psi_f \sim U[-1, 1]$. Parameterize the wavefunction as $\Psi_f \rightarrow (\cos \theta/2, e^{i\phi} \sin \theta/2)^T$, the transmission probabilities are:

$$T_{ee} = \cos^2 \frac{\theta}{2} = \frac{1+z}{2} \sim U[0, 1], \quad T_{eh} = \sin^2 \frac{\theta}{2} = \frac{1-z}{2} \sim U[0, 1], \quad T = T_{ee} - T_{eh} = \cos \theta = z \sim U[-1, 1], \quad (\text{S21})$$

all follow continuous uniform distributions.

Case (iii): QAH-SC-QAH junction with $N = 1$ as shown in Fig. 1(d):

Near the corners of the TSC region, the effective Hamiltonian is: $H_{\text{TSC}} = vk\tau_0 - \eta\tau_z + \Delta k\tau_x$ in the Nambu basis [12]. Away from the corners, $\eta = 0$. This Hamiltonian is the same as the effective Hamiltonian for $N = 2$ TSC, as long as μ is replaced by η . Therefore, the analyses in Appendix I and above are still valid.

Considering the configuration of Fig. 1(d) in the main text, the final state is: $\Psi_f = Q'M'S_{23}M\Lambda Q\Psi_i$, where the initial and final states are now four-component vectors. M transforms electron basis to Majorana basis:

$$M = \frac{1}{\sqrt{2}} \begin{pmatrix} 1 & 1 & 0 & 0 \\ -i & i & 0 & 0 \\ 0 & 0 & 1 & 1 \\ 0 & 0 & -i & i \end{pmatrix}, \quad (\text{S22})$$

under the basis $(c^\dagger, c, c'^\dagger, c')^T$. $M' = M^{-1}$. S_{23} braids two Majorana modes γ_2 and γ_3 as:

$$S_{23} = \begin{pmatrix} 1 & 0 & 0 & 0 \\ 0 & 0 & 1 & 0 \\ 0 & -1 & 0 & 0 \\ 0 & 0 & 0 & 1 \end{pmatrix}. \quad (\text{S23})$$

Λ accounts for the propagation process away from the corners, which is a diagonal matrix, whose diagonal elements are all phase factors. Q, Q' represent the propagation process near the corners, which are block diagonal, each block is the product of several \mathbb{T}_ℓ matrices:

$$Q = \begin{pmatrix} a_{11} & a_{12} & 0 & 0 \\ a_{21} & a_{22} & 0 & 0 \\ 0 & 0 & b_{11} & b_{12} \\ 0 & 0 & b_{21} & b_{22} \end{pmatrix}, \quad Q' = \begin{pmatrix} d_{11} & d_{12} & 0 & 0 \\ d_{21} & d_{22} & 0 & 0 \\ 0 & 0 & c_{11} & c_{12} \\ 0 & 0 & c_{21} & c_{22} \end{pmatrix}, \quad (\text{S24})$$

where the block matrix a is:

$$a = \begin{pmatrix} a_{11} & a_{12} \\ a_{21} & a_{22} \end{pmatrix} = \mathbb{T}_L \cdots \mathbb{T}_2 \mathbb{T}_1 = \mathbb{T} \propto e^{\frac{i\alpha(\mathbf{n} \cdot \boldsymbol{\sigma})}{2}}, \quad (\text{S25})$$

and similar for b, c, d matrices. As indicated by Fig. 1(d) in the main text, the two incoming electrons are phase-incoherent, so the charge transmission fraction from lead 2 to 3 [T in Eq. (S8)] is obtained by setting $\Psi_i = (1, 0, 0, 0)^T$ then calculating the first two components of Ψ_f ; and the charge transmission fraction from lead 5 to 3 [R in Eq. (S8)] is obtained by setting $\Psi_i = (0, 0, 1, 0)^T$ then calculating the first two components of Ψ_f . The final result is:

$$T = T_{ee} - T_{eh} = \frac{1}{4} |a_{11} + a_{21}|^2 (|d_{11} + d_{12}|^2 - |d_{21} + d_{22}|^2), \quad (\text{S26})$$

$$R = R_{ee} - R_{eh} = \frac{1}{4} |b_{11} + b_{21}|^2 (|d_{11} - d_{12}|^2 - |d_{21} - d_{22}|^2).$$

From Eq. (S25):

$$|a_{11} \pm a_{21}|^2 = 1 \pm n_x n_y - \mp n_x n_z \cos \alpha \mp n_y \sin \alpha. \quad (\text{S27})$$

Due to the finite decay length of the edge modes wavefunction, $\eta \neq 0$ only near the corner, thus the L in Eq. (S25) is small, resembling Case (i). Expanding around \bar{a} up to the first order, $|a_{11} + a_{21}|^2 \sim \bar{a} - \delta a$ is normal distributed with small variance. $|a_{11} - a_{21}|^2$, $|b_{11} \pm b_{21}|^2$, etc. yield similar results. Then $|a_{11} + a_{21}|^2 |d_{11} + d_{12}|^2 \sim \bar{a}\bar{d} + \bar{a}\delta d + \bar{d}\delta a$ is also normal distributed, up to the first order. Therefore, T_{ee} , T_{eh} , R_{ee} , R_{eh} , and thus T , R are all normal distributed with small variance. The above analysis reveals that the transmission probability is independent of L , which results from the incoherence of incident electrons, making the phase accumulation in Λ no effect on the final result.

Case (iv): \mathbf{n}_ℓ is fixed, and the number of sections L is large.

This case resembles Case (i) except L is sufficiently large, then the fluctuation of the total rotation angle, i.e., σ is large. One can expand Eq. (S17) using Fourier series:

$$f_w(\alpha') = \frac{1}{2\pi} \sum_{n=-\infty}^{\infty} e^{in(\alpha' - \bar{\alpha}') - \frac{\sigma^2 n^2}{2}}. \quad (\text{S28})$$

When $\sigma \rightarrow \infty$, only $n = 0$ term gives nonzero contribution, thus $f_w(\alpha')$ becomes a constant $1/(2\pi)$, meaning that α' follows a uniform distribution $U[0, 2\pi]$. Thus Eq. (S18) approaches:

$$f(T) = \begin{cases} \frac{1}{\pi(1-A)\sqrt{1-\left(\frac{T-A}{1-A}\right)^2}}, & T \in [1-2A, 1] \\ 0, & \text{otherwise} \end{cases}. \quad (\text{S29})$$

which is an arcsine distribution on the interval $[1-2A, 1]$, a shifted and rescaled variant of the standard arcsine distribution.

IV. DECOHERENCE EFFECT AND PARTICLE LOSS

A. Decoherence

We first consider the decoherence effect. Phenomenologically, we can incorporate the decoherence effect of the edge mode in the TSC region by introducing floating leads [13] at the boundaries of the TSC region, which acts as decoherence sources. If the superconducting coherent length is comparable to the junction length, we can assume that there is only one floating lead at the edge of the TSC region. We introduce a parameter p to describe the probability that edge modes enter a floating lead in the TSC region.

For the QAH-SC-QAH junction shown in Fig. S1(b), part of Eq. (S8) is modified:

$$\begin{aligned} I_d &= \frac{e^2}{h} [(V_d - V_s) + p_d T_d^{(1)} (V_s - V_2)] = 0, & I_r &= \frac{e^2}{h} [(V_r - V_s) + p_r R_r^{(1)} (V_s - V_5)] = 0, \\ I_3 &= \frac{e^2}{h} [(V_3 - V_s) + p_d T_d^{(2)} (V_s - V_d) + (1 - p_d) T_d^{(1,2)} (V_s - V_2) + p_r R_r^{(2)} (V_s - V_r) + (1 - p_r) R_r^{(1,2)} (V_s - V_5)], \\ I_u &= \frac{e^2}{h} [(V_u - V_s) + p_u T_u^{(1)} (V_s - V_5)] = 0, & I_l &= \frac{e^2}{h} [(V_l - V_s) + p_l R_l^{(1)} (V_s - V_2)] = 0, \\ I_6 &= \frac{e^2}{h} [(V_6 - V_s) + p_u T_u^{(2)} (V_s - V_u) + (1 - p_u) T_u^{(1,2)} (V_s - V_5) + p_l R_l^{(2)} (V_s - V_l) + (1 - p_l) R_l^{(1,2)} (V_s - V_2)], \end{aligned} \quad (\text{S30})$$

where p_d and $1 - p_d$ are the probability of the edge modes entering and not entering the floating lead d , respectively. $T_d^{(1)}$ is the charge transmission fraction from lead 2 to lead d , $T_d^{(2)}$ is from lead d to lead 3, $T_d^{(1,2)}$ is from lead 2 to lead 3, which is the original coherent process. Other symbols have similar interpretations. Therefore:

$$I_3 = \frac{e^2}{h} [(V_3 - V_s) + T_d^{\text{tot}} (V_s - V_2) + R_r^{\text{tot}} (V_s - V_5)], \quad I_6 = \frac{e^2}{h} [(V_6 - V_s) + T_u^{\text{tot}} (V_s - V_5) + R_l^{\text{tot}} (V_s - V_2)], \quad (\text{S31})$$

where the effective charge transmission fractions are:

$$\begin{aligned} T_d^{\text{tot}} &= (1 - p_d) T_d^{(1,2)} + p_d T_d^{(1)} T_d^{(2)}, & R_r^{\text{tot}} &= (1 - p_r) R_r^{(1,2)} + p_r R_r^{(1)} R_r^{(2)}, \\ T_u^{\text{tot}} &= (1 - p_u) T_u^{(1,2)} + p_u T_u^{(1)} T_u^{(2)}, & R_l^{\text{tot}} &= (1 - p_l) R_l^{(1,2)} + p_l R_l^{(1)} R_l^{(2)}. \end{aligned} \quad (\text{S32})$$

Consequently, one can include the decoherence effect by replacing the charge transmission fractions with the corresponding effective ones.

For the QAH-SC junction shown in Fig. S1(c), we first consider $N = 2$ case, where the the upper route is absent, part of Eq. (S13) is modified:

$$I_d = \frac{e^2}{h} [(V_d - V_s) + p_d T_d^{(1)} (V_s - V_2)] = 0, \quad I_3 = \frac{e^2}{h} [(V_3 - V_s) + p_d T_d^{(2)} (V_s - V_d) + (1 - p_d) T_d^{(1,2)} (V_s - V_2)]. \quad (\text{S33})$$

Eliminating V_d , T_d^{tot} is the same as the QAH-SC-QAH junction case, i.e., Eq. (S32). $N = 1$ case is slightly complicated: if p_d and p_u represent the probabilities of edge mode entering the floating lead d and u , respectively, the coherent component is $\min(1 - p_d, 1 - p_u)$, and the remaining part $|p_u - p_d|$ is the incoherent component of the transport process directly from lead 2 to 3. Part of Eq. (S13) should be modified as:

$$I_d = \frac{e^2}{h} [(V_d - V_s) + p_d T_d^{(1)} (V_s - V_2)] = 0, \quad I_u = \frac{e^2}{h} [(V_u - V_s) + p_u T_u^{(1)} (V_s - V_2)] = 0, \quad (\text{S34})$$

$$I_3 = \frac{e^2}{h} \left[(V_3 - V_s) + \left(p_d T_d^{(1)} T_d^{(2)} + p_u T_u^{(1)} T_u^{(2)} + |p_u - p_d| T_{\text{inco}} + \min(1 - p_d, 1 - p_u) T_{\text{co}} \right) (V_s - V_2) \right].$$

Therefore:

$$T_d^{\text{tot}} = p_d T_d^{(1)} T_d^{(2)} + p_u T_u^{(1)} T_u^{(2)} + |p_u - p_d| T_{\text{inco}} + \min(1 - p_d, 1 - p_u) T_{\text{co}}. \quad (\text{S35})$$

Note that the transport process $T_d^{(1)}$, $T_d^{(2)}$, $T_u^{(1)}$, $T_u^{(2)}$ and T_{inco} corresponding to single Majorana mode transmission from one lead to another, which are analogous to, e.g., the charge transmission process T_d in QAH-SC-QAH junction with $N = 1$ without decoherence effect. Thus they follow normal distribution when taking into account of the disorder effect.

In the following, we focus on the long junction case, where each charge transmission fraction converges to the form of its large L limit. Without loss of generality, we take T_d^{tot} as an example. For $N = 2$ case, $T_d^{(1,2)}$, $T_d^{(1)}$ and $T_d^{(2)}$ in Eq. (S32) all follow $U[-1, 1]$, one can obtain the analytical result of T_d^{tot} . When $p \leq 0.5$:

$$f(T) = \begin{cases} -\frac{1}{2(p-1)}, & |T| \leq 1 - 2p \\ \frac{1}{4(p-1)p} \left[|T| + (p + |T| - 1) \log \left(\left| \frac{p}{p+|T|-1} \right| \right) - 1 \right], & 2p - 1 < |T| \leq 1. \\ 0, & \text{otherwise} \end{cases} \quad (\text{S36})$$

Apparently, when $p = 0$, $f(T)$ reduces to constant $1/2$ over $[-1, 1]$. For $p > 0.5$:

$$f(T) = \begin{cases} \frac{1}{4(p-1)p} \left[(|T| - p + 1) \log \left(\frac{|T| - p + 1}{p} \right) + (|T| + p - 1) \log \left(\frac{p}{|p+|T|-1} \right) + 2(p - 1) \right], & |T| < 2p - 1 \\ \frac{1}{4(p-1)p} \left[|T| + (p + |T| - 1) \log \left(\left| \frac{p}{p+|T|-1} \right| \right) - 1 \right], & 2p - 1 \leq |T| \leq 1, \\ 0, & \text{otherwise} \end{cases} \quad (\text{S37})$$

and when $p = 1$, $f(T)$ becomes $-\frac{1}{2} \log |T|$ over $[-1, 1]$. We plot this probability density function in Figs. S2(a-d), which show that increasing p causes the distribution of T to become more concentrated around zero, and when $p = 1$, $f(T)$ becomes logarithmic divergence. For $N = 1$ case, the distribution of T_d^{tot} is far more complicated, while one can find analytical result for $T_d^{(1)} T_d^{(2)}$, which is product two independent and identically distributed Gaussian random variables. The probability density function is [14]:

$$f(T = T_d^{(1)} T_d^{(2)}) = e^{-\frac{\mu^2}{\sigma^2}} \sum_{n=0}^{\infty} \sum_{m=0}^{2n} \binom{2n}{m} \frac{\mu^{2n} T^{2n-m} |T|^{m-n}}{\pi (2n)! \sigma^{4n+2}} K_{m-n} \left(\frac{|T|}{\sigma^2} \right), \quad (\text{S38})$$

where K_v denotes the modified Bessel function of the second kind and order v . The final effective transmission fraction will be a mixture of the above distribution and normal and (or) arcsine distribution, depending on the concrete configuration. We show the results for QAH-SC-QAH junction with $N = 1$ case in Fig. S2(f-i), and QAH-SC junction with $N = 1$ case in Fig. S2(k-n), where, for simplicity, we assume $p_d = p_u = p$ and the same distribution for $T_d^{(1)}$, $T_d^{(2)}$, $T_u^{(1)}$, $T_u^{(2)}$, and T_{inco} . One can find that when p is small, the distributions are similar to that without decoherence effect. When $p \rightarrow 1$, $f(T)$ in both cases converge to Eq. (S38).

If the coherent length is shorter, more floating leads need to be introduced, dividing the TSC region into several segments, the resulting multi-terminal formula is more complicated. While at this situation, one can reasonably assume that $p = 1$, which means edge modes will flow into every floating lead and totally lose coherence. For $N = 2$

case and QAH-SC-QAH junction with $N = 1$ case, the effective transmission fraction is simply the product of charge transmission fraction for each section [15]:

$$T^{\text{tot}} = T_{a,1} T_{1,2} \cdots T_{m,b}, \quad (\text{S39})$$

when there are m leads at the edge, where the subscripts a and b means the actual leads on both sides, and subscripts 1 to m represent virtual floating leads. For QAH-SC junction with $N = 1$, the effective transmission fraction is the sum of two path:

$$T^{\text{tot}} = T_{a,1}^u T_{1,2}^u \cdots T_{m,b}^u + T_{a,1}^d T_{1,2}^d \cdots T_{m,b}^d. \quad (\text{S40})$$

For $N = 2$ case one can obtain analytical result for the distribution of T^{tot} when charge transmission fraction for each section satisfies $U[-1, 1]$:

$$f(T = T^{\text{tot}}) = \frac{(-1)^m}{2(m)!} [\log(|T|)]^m. \quad (\text{S41})$$

In Fig. S2(e,j) we plot the results for $N = 2$, QAH-SC-QAH junction with $N = 1$, respectively (the result for QAH-SC junction with $N = 1$ is similar to that for QAH-SC-QAH junction with $N = 1$, and is not shown here). When more floating leads are introduced, $f(T^{\text{tot}})$ in $N = 2$ case still peaks at zero value, but the divergence rate increases, while $f(T^{\text{tot}})$ in $N = 1$ case remains bell-shaped like, but becomes more concentrated with a decrease of in the peak value of T^{tot} .

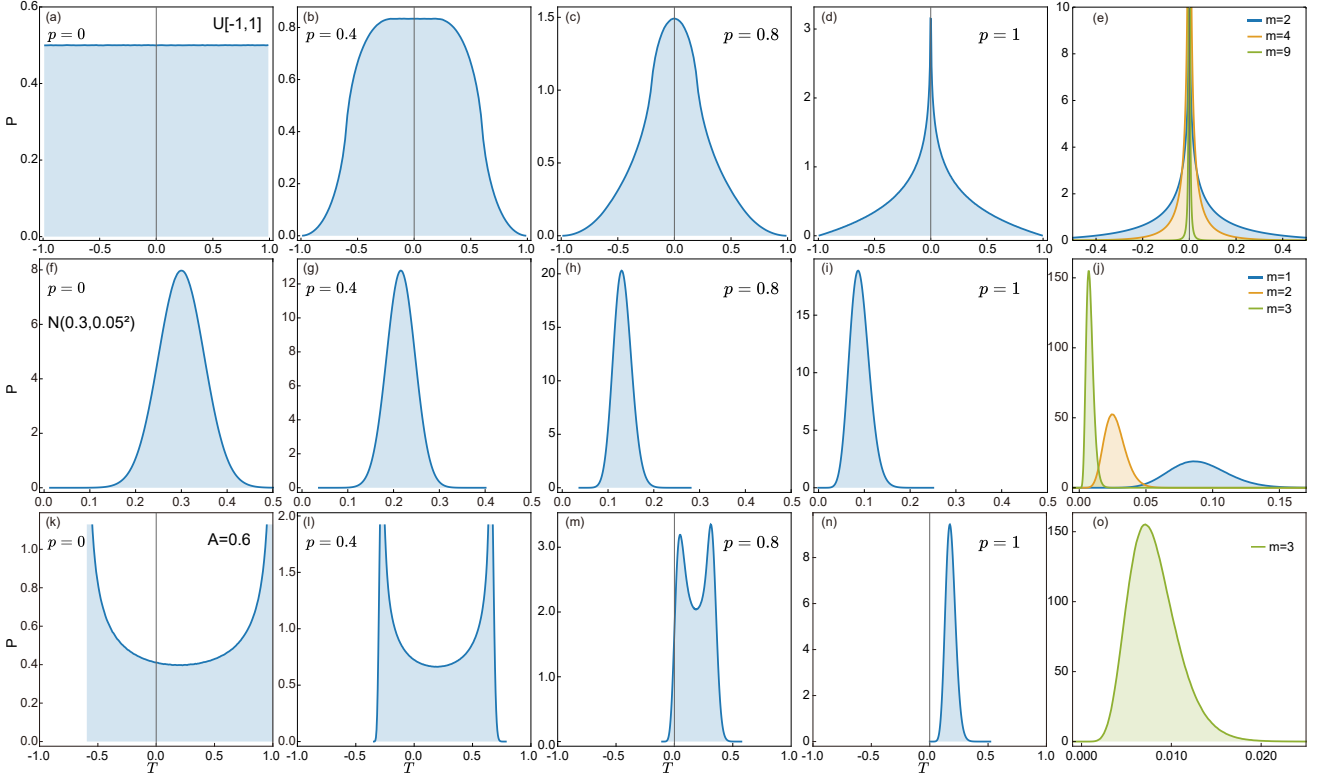


FIG. S2. Decoherence effect on the probability distribution of transmission fraction. We generate 10^7 random numbers for the charge transmission fraction of each subsegment, then calculate effective charge transmission fraction and obtain its distribution numerically. (a-e) $N = 2$ case, using Eq. (S32). The charge transmission fraction for each segment satisfies $U[-1, 1]$. In (a-d) there is one floating lead, and in (e) there are multiple floating leads. (f-j) QAH-SC-QAH junction with $N = 1$, using Eq. (S32). The charge transmission fraction for each segment satisfies $\mathcal{N}(0.3, 0.05^2)$. In (f-i) there is one floating lead, and in (j) there are multiple floating leads. (o) is horizontally scaled version of (j) when there are three floating leads. (k-n) QAH-SC junction with $N = 1$, using Eq. (S35). We set $p_u = p_d = p$, $T_d^{(1)}$, $T_d^{(2)}$, $T_u^{(1)}$, $T_u^{(2)}$, T_{inco} follow $\mathcal{N}(0.3, 0.05^2)$, and T_{co} follows an arcsine distribution with $A = 0.6$.

B. Particle loss

The phenomenological treatment of particle loss is straightforward. Since it is the process that particles escape from the device, one can introduce a parameter q taking values between 0 to 1 to describe the reduction of the particle number: $\Psi_f = q^m \Psi_f^0 = e^{m \log q} \Psi_f^0$, where m is the number of vortices, Ψ_f^0 is the state without particle loss process. This factor merely reduces the amplitude of T , indicating that particle loss compresses the distribution of T , without altering its overall shape. Therefore, particle loss effect does not change the qualitative results of this work.

V. TECHNICAL DETAILS OF NUMERICAL CALCULATIONS

In the numerical calculations presented in the main text, we consider the QAH state in a magnetic topological insulator thin film with ferromagnetic order. The two-dimensional effective Hamiltonian is $\mathcal{H}_0 = \sum_{\mathbf{k}} \psi_{\mathbf{k}}^\dagger H_0(\mathbf{k}) \psi_{\mathbf{k}}$, where $\psi_{\mathbf{k}} = (c_{\mathbf{k}\uparrow}^t, c_{\mathbf{k}\downarrow}^t, c_{\mathbf{k}\uparrow}^b, c_{\mathbf{k}\downarrow}^b)^T$ and $H_0(\mathbf{k}) = k_y \sigma_x \tau_z - k_x \sigma_y \tau_z + m(\mathbf{k}) \tau_x + \lambda \sigma_z$. Here, the superscripts t and b denote the top and bottom surface states, respectively. σ_i and τ_i are Pauli matrices for spin and layer, respectively. λ is the exchange field. $m(\mathbf{k}) = m_0 + m_1(k_x^2 + k_y^2)$ represents the hybridization between the top and bottom surface states. This model accurately describes the QAH state in Cr-doped $(\text{Bi,Sb})_2\text{Te}_3$ [16] and odd-layer MnBi_2Te_4 [17]. The chiral TSC is induced by superconducting proximity of the QAH state [18], with the effective BdG Hamiltonian $\mathcal{H}_{\text{bulk}} = \sum_{\mathbf{k}} \Psi_{\mathbf{k}}^\dagger H_{\text{bulk}}(\mathbf{k}) \Psi_{\mathbf{k}}/2$, where $\Psi_{\mathbf{k}} = [(c_{\mathbf{k}\uparrow}^t, c_{\mathbf{k}\downarrow}^t, c_{\mathbf{k}\uparrow}^b, c_{\mathbf{k}\downarrow}^b), (c_{-\mathbf{k}\uparrow}^{t\dagger}, c_{-\mathbf{k}\downarrow}^{t\dagger}, c_{-\mathbf{k}\uparrow}^{b\dagger}, c_{-\mathbf{k}\downarrow}^{b\dagger})]^T$ and

$$H_{\text{bulk}}(\mathbf{k}) = \begin{pmatrix} H_0(\mathbf{k}) - \mu & \Delta(\mathbf{k}) \\ \Delta(\mathbf{k})^\dagger & -H_0^*(-\mathbf{k}) + \mu \end{pmatrix}, \quad \Delta(\mathbf{k}) = \begin{pmatrix} i\Delta_t \sigma_y & 0 \\ 0 & i\Delta_b \sigma_y \end{pmatrix}. \quad (\text{S42})$$

Here, μ is the chemical potential, and Δ_t and Δ_b are the pairing gap functions on the top and bottom surface states, respectively. The topological properties of this system were well studied in Ref. [18], revealing three TSC phases with BdG Chern numbers $N = 0, 1, 2$.

We set $v = 1$, $\mu = 0.2$, $m_0 = 1$, $m_1 = 1.5$, and $\lambda = 5$ for the QAH, $\Delta_t = 1$, $\Delta_b = 0$, $\lambda = 1.1$ for the $N = 1$ TSC, $\lambda = 3$ for the $N = 2$ TSC. To ensure the edge modes along the two boundaries do not overlap, the width of the junction is $30a$ with $a \equiv 1$ as the lattice constant. The disorder effect in the TSC region is considered by making μ a random field, which follows a uniform distribution $\mu \in U[-W_{\text{dis}}/2, W_{\text{dis}}/2]$, with W_{dis} the strength of the disorder potential. We have verified that using a Gaussian-distributed disorder potential does not alter the conclusions of this study. Since the interface between quantum Hall or QAH insulator and superconductor is highly inhomogeneous, we consider short-range disorder with disorder correlation length $\xi_d = a$, i.e., every lattice site has a random μ independent of each other. In the main text, we set $W_{\text{dis}} = 0.2$. By calculating a sufficient number of different disorder configurations, we obtain the distribution of transmission. We use 1×10^4 configurations when plotting the distribution and 500 configurations when plotting the transmission (reflection)-length relation.

In the calculation of transmission fraction, we adopt the recursive Green's function method [19–23]. The effect of the semi-infinite lead on the center region (TSC region) is manifested in the form of self-energy. The center region is divided into columns, and using the recursive algorithm, one can obtain the Green's function of the center region. At zero temperature, the normal (T_{ee}) and anomalous (T_{eh}) transmission probabilities from lead i to j are calculated by [24]:

$$T_{j,e \leftarrow i,e} = \text{Tr}([\Gamma_j]_{\text{ee}}[G_c]_{\text{ee}}[\Gamma_i]_{\text{ee}}[G_c^\dagger]_{\text{ee}}), \quad T_{j,h \leftarrow i,e} = \text{Tr}([\Gamma_j]_{\text{hh}}[G_c]_{\text{he}}[\Gamma_i]_{\text{ee}}[G_c^\dagger]_{\text{eh}}), \quad (\text{S43})$$

respectively, where $\Gamma_j = i(\Sigma_j - \Sigma_j^\dagger)$, G_c is the Green's function of i of the center region, Σ_j is the self-energy for lead j , and the subscripts e (h) denote the electron (hole) sector of the matrix.

VI. NUMERICAL RESULTS

A. Numerical results for QAH-SC-QAH junction

In addition to Fig. 2 and Fig. 3 in the main text, we present more numerical results for the QAH-SC-QAH junction. Fig. S3 shows the $T - L$ relation for the $N = 2$ case under different incident electron energies and disorder potential strengths from the main text. These results are consistent with Fig. 2 in the main text, with only the oscillation amplitude and decay length differing due to different parameters. The distributions of T at different L are shown in Fig. S4. These results further support the conclusions made in the main text. As L increases, the fluctuation of T

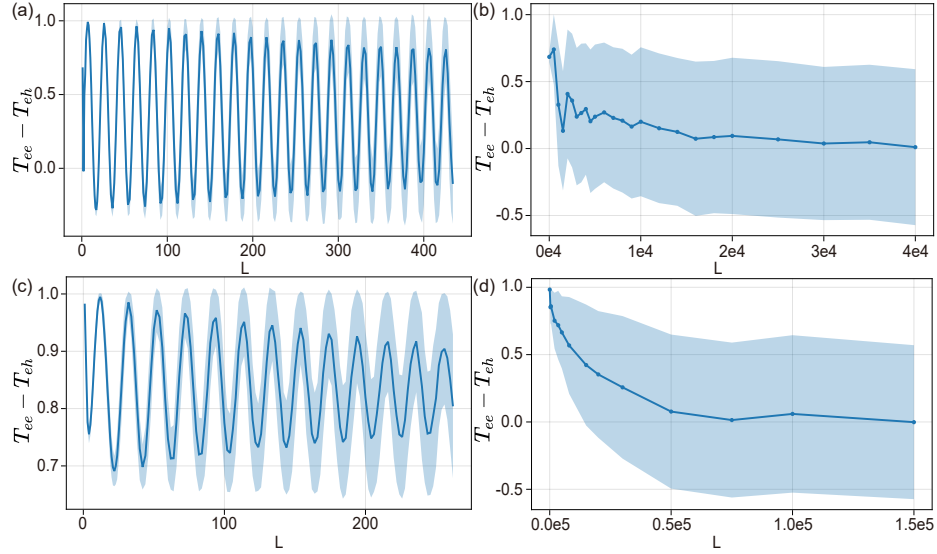


FIG. S3. The relation of charge transmission and the length of the TSC region for the QAH-SC-QAH junction with $N = 2$. (a)(b) $\varepsilon = 0.63$, $W_{\text{dis}} = 0.1$ case. (c)(d) $\varepsilon = 0.4$, $W_{\text{dis}} = 0.2$ case. The blue shading represents one standard deviation.

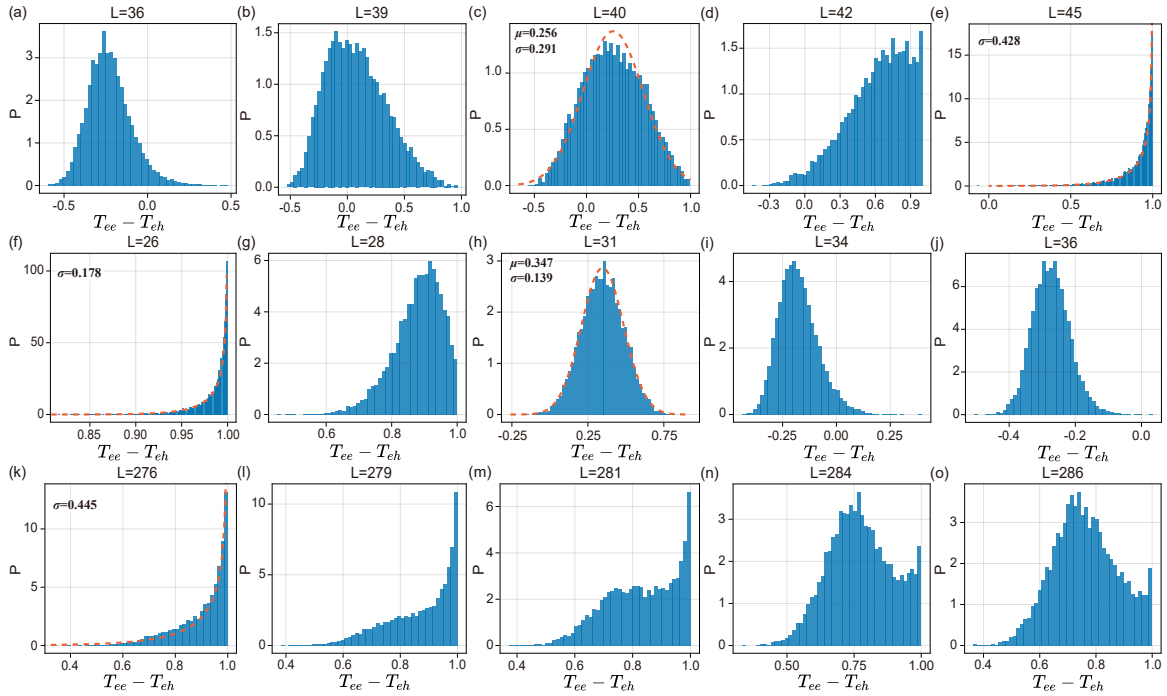


FIG. S4. The distribution of charge transmission for the QAH-SC-QAH junction with $N = 2$. (a-e) $\varepsilon = 0.63$, $W_{\text{dis}} = 0.2$ case. (f-j) $\varepsilon = 0.63$, $W_{\text{dis}} = 0.1$ case. (k-o) $\varepsilon = 0.4$, $W_{\text{dis}} = 0.2$ case. The orange dashed lines in some figures are the fitting curves when the distribution is close to normal or chi-squared distribution.

increases. Since T is always bounded within $[-1, 1]$, the resulting distribution deviates from the normal or chi-squared distribution when L is large.

For the $N = 1$ case, the $R - L$ relation is shown in Fig. S5(a), which exhibits similar behavior to T shown in the main text. As a supplement, the $T - L$ and $R - L$ relations in the clean case are shown in Fig. S5(b) and Fig. S5(c). The distributions of T and R are always Gaussian as long as L is large enough to avoid overlap of wavefunctions for edge modes on opposite sides, regardless of different parameters. This is confirmed by Fig. S5(d-i).

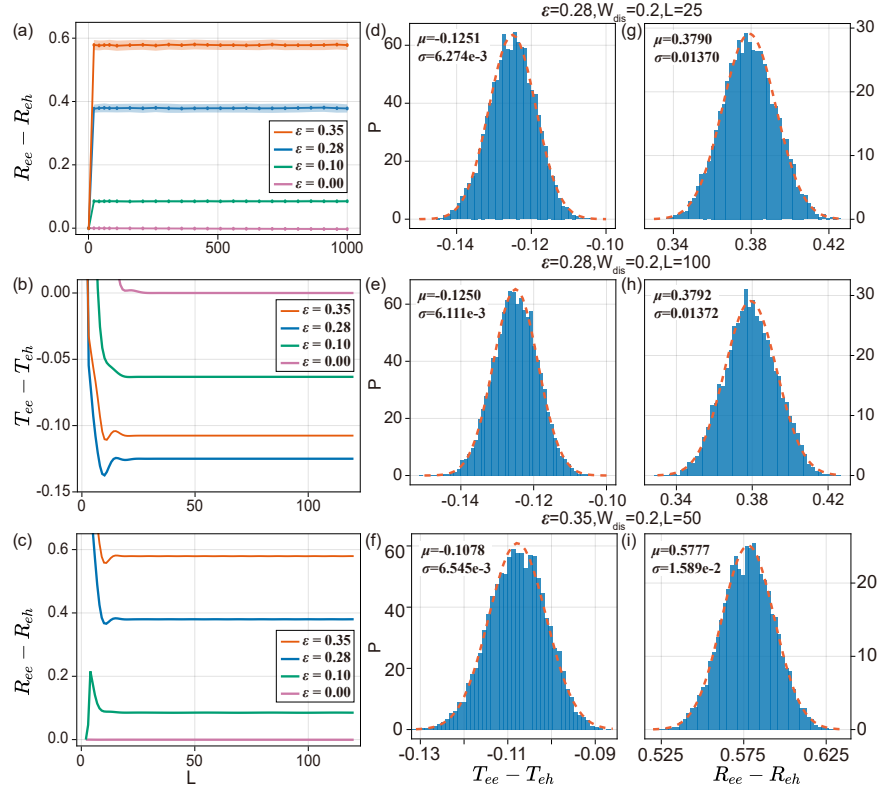


FIG. S5. The distribution of charge transmission (reflection) for the QAH-SC-QAH junction with $N = 1$. (a) $R - L$ relation. (b) and (c) are $T - L$ and $R - L$ relations without disorder. (d-f) The distribution of T at different L or ε , and that of R is shown in (g-i). The orange dashed lines are the fitting Gaussian curves.

B. Numerical results for QAH-SC junction

In addition to Fig. 3 in the main text, we present further numerical results for the QAH-SC junction. For the $N = 2$ case, the $T - L$ relationship is shown in Fig. S6. This is nearly identical to the QAH-SC-QAH junction with $N = 2$, as the transmission processes from lead 2 to 3 are exactly the same. The corresponding distribution of T is also the same, thus not shown here. Fig. S7 shows the distributions of T at small L with the same parameter setup as in Fig. 3(c,d) in the main text. The results support the conclusion of Case (i) in the main text. Another parameter setup for the $N = 1$ case is shown in Fig. S8. Only the oscillation amplitude and decay length differ from Fig. 3(c,d) in the main text. As L increases, the distribution deviates from a normal or chi-squared distribution, gradually approaching a generalized arcsine distribution.

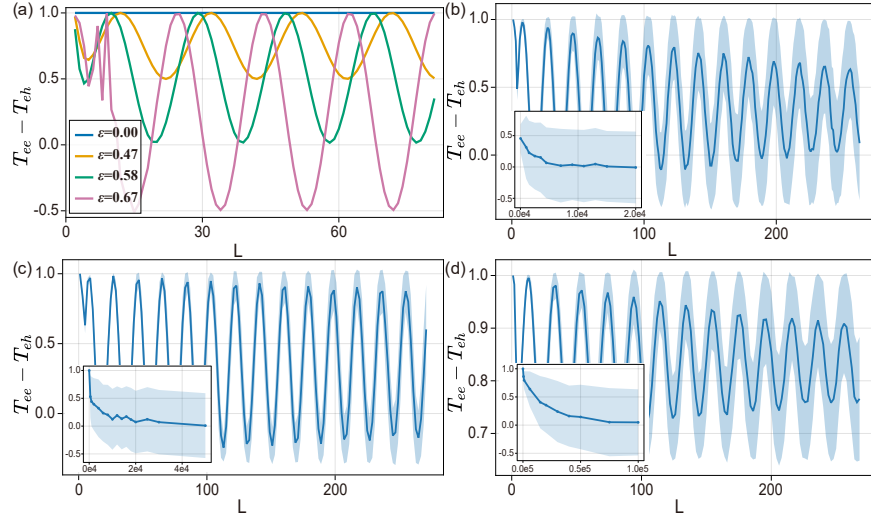


FIG. S6. The relationship between charge transmission and the length of the TSC region for the QAH-SC junction with $N = 2$. (a) Disorder-free case. (b) $\varepsilon = 0.63$, $W_{\text{dis}} = 0.2$ case. (c) $\varepsilon = 0.63$, $W_{\text{dis}} = 0.1$ case. (d) $\varepsilon = 0.4$, $W_{\text{dis}} = 0.2$ case. Insets in (b-d) show the corresponding large L cases. The blue shading represents one standard deviation.

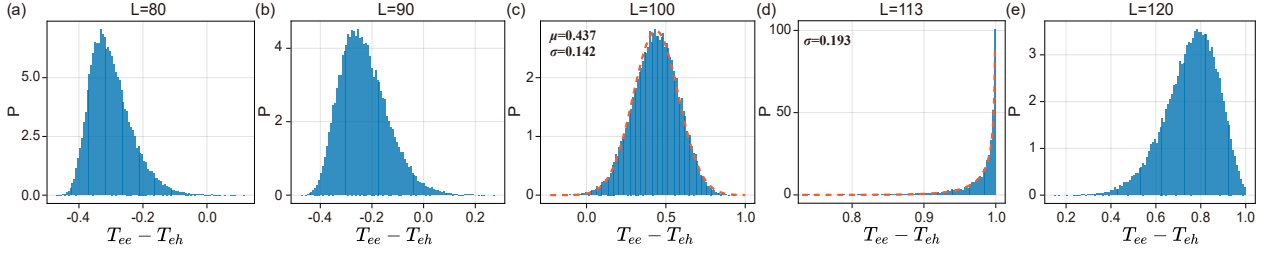


FIG. S7. The distribution of charge transmission for the QAH-SC junction with $N = 1$. The parameters are the same as in Fig. 3(c,d) in the main text. The orange dashed lines in some figures are the fitting curves when the distribution is close to the normal or chi-squared distribution.

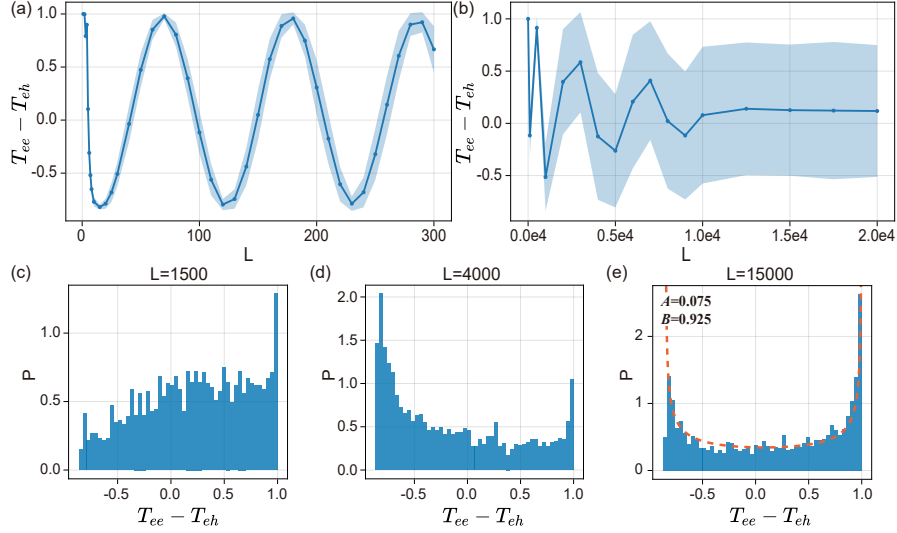


FIG. S8. The case of $\varepsilon = 0.18$, $W_{\text{dis}} = 0.3$ for the QAH-SC junction with $N = 1$. (a)(b) The relationship between charge transmission and the length of the TSC region. The blue shading represents one standard deviation. (c-e) The distribution of charge transmission. The orange dashed lines in (e) are the fitting curves.

C. Numerical results for $N = 0$ cases

When the SC region of the junction is topologically trivial, i.e., $N = 0$, two chiral Bogoliubov edge modes emerge along the interface between SC and QAH, thus the edge modes transport characteristics is analogous to the $N = 2$ case, where those modes emerge along the interface between SC and vacuum. In QAH-SC-QAH junction, T is always zero due to the absence of edge modes at the SC/vacuum interface. While one can observe the oscillation of charge reflection fraction R with the width W of the junction, as Andreev conversion occurs at the SC/QAH interface, see Fig. S9(a). In QAH-SC junction, the edge modes are shown in Fig. S10(a), allowing investigation of the charge transmission fraction, similar to the $N = 2$ case.

We provide numerical calculations for both cases. The effective Hamiltonian for the QAH is:

$$\mathcal{H}_{\text{QAH}} = \sum_{\mathbf{k}} c_{\mathbf{k}}^{\dagger} [\zeta(\mathbf{k}) \cdot \boldsymbol{\sigma} - \mu_h] c_{\mathbf{k}}, \quad (\text{S44})$$

and the BdG Hamiltonian for the NSC is:

$$\mathcal{H}_{\text{SC}} = \sum_{\mathbf{k}} \Psi_{\mathbf{k}}^{\dagger} [\epsilon(\mathbf{k}) - \mu_s] \Psi_{\mathbf{k}} + (\Delta \Psi_{\mathbf{k}}^T i \sigma_y \Psi_{-\mathbf{k}} + \text{H.c.}). \quad (\text{S45})$$

where $\Psi_{\mathbf{k}} = (c_{\mathbf{k}\uparrow}, c_{\mathbf{k}\downarrow})^T$, $\zeta(\mathbf{k}) = [M - B(\cos k_x a + \cos k_y a), A \sin k_x a, A \sin k_y a]$, $\boldsymbol{\sigma} = (\sigma_x, \sigma_y, \sigma_z)$ are the Pauli matrices, $\epsilon(\mathbf{k}) = B(2 - \cos k_x a - \cos k_y a)$ is the kinetic energy, a is the lattice constant, Δ is the pairing amplitude, and μ_h and μ_s are the chemical potentials of the QAH and the NSC, respectively [25]. The parameters are chosen as: $a = 0.8$, $B = 1.5625$, $M = 2.625$, $A = 1.25$, $\Delta = 0.3$, $\mu_h = 0.2$, and $\mu_s = 0.5$. The number of disorder configurations is 500.

The numerical results are shown in Figs. S9 and S10. The main tendencies of charge reflection (transmission) are

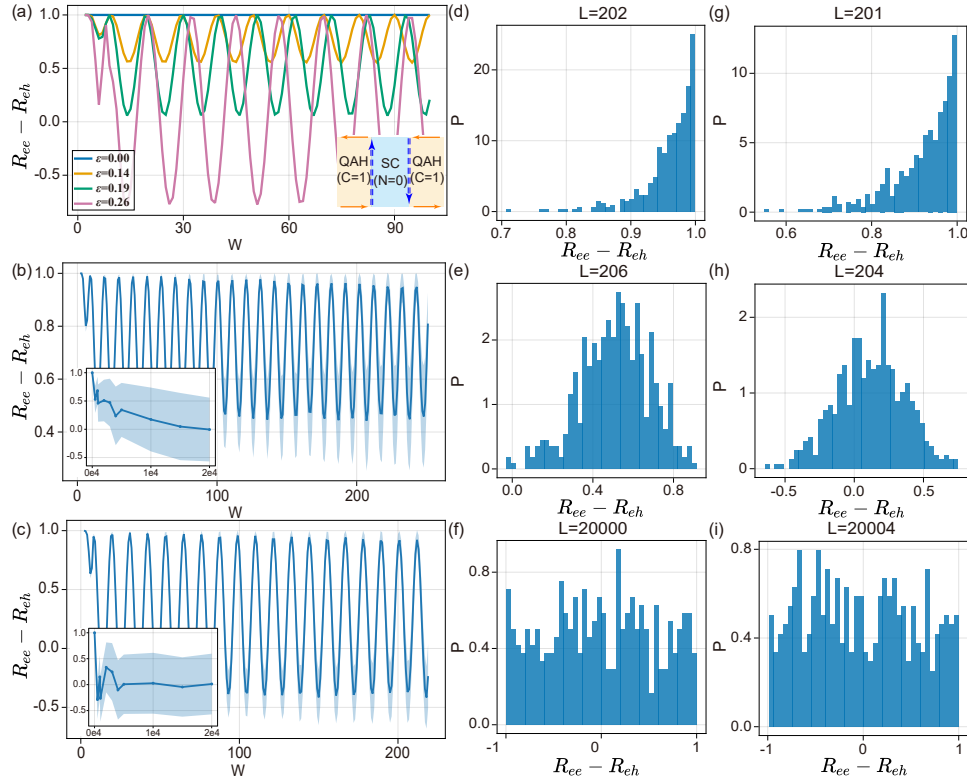


FIG. S9. Charge reflection for the QAH-NSC-QAH junction. (a-c) Relationship between charge reflection and the width of the junction. (d-i) Distribution of charge reflection. (a) Disorder-free case. Inset shows the schematic diagram of the device. (b) and (d-f) $\epsilon = 0.15$, $W_{\text{dis}} = 0.2$ case. (c) and (g-i) $\epsilon = 0.23$, $W_{\text{dis}} = 0.2$ case. The blue shading represents one standard deviation.

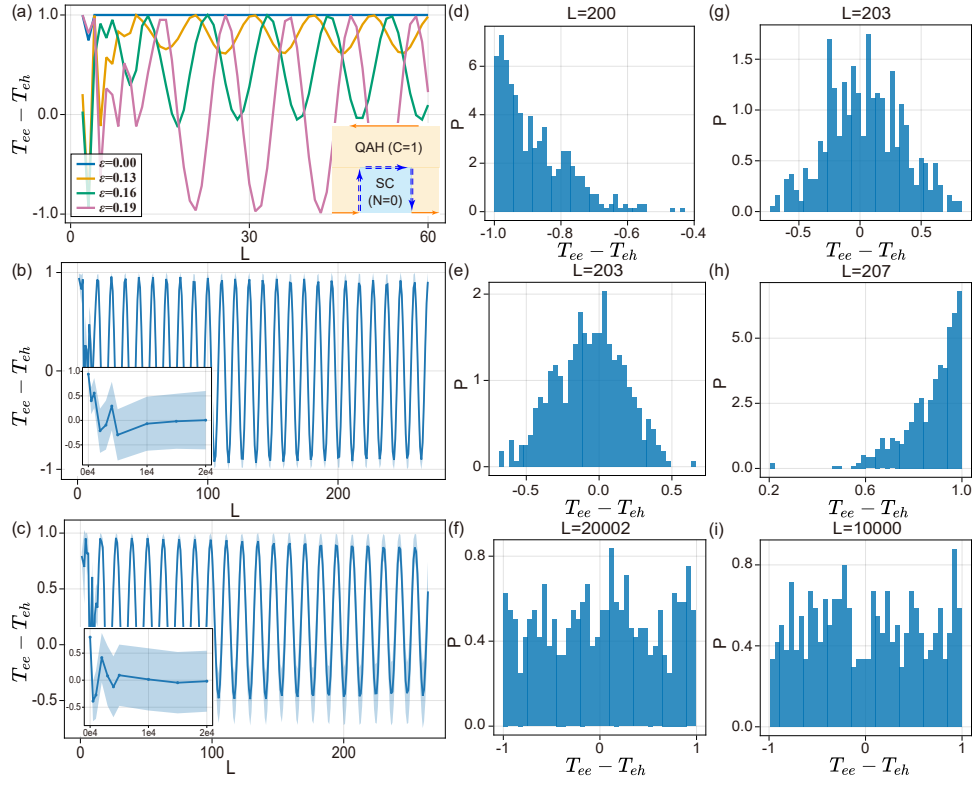


FIG. S10. Charge transmission for the QAH-NSC junction. (a-c) Relationship between charge transmission and the length of the junction. (d-i) Distribution of charge transmission. (a) Disorder-free case. Inset shows the schematic diagram of the device. (b) and (d-f) $\varepsilon = 0.19$, $W_{\text{dis}} = 0.2$ case. (c) and (g-i) $\varepsilon = 0.25$, $W_{\text{dis}} = 0.2$ case. The blue shading represents one standard deviation.

quite similar to those for the $N = 2$ case.

-
- [1] J. A. M. van Ostaay, A. R. Akhmerov, and C. W. J. Beenakker, Spin-triplet supercurrent carried by quantum hall edge states through a josephson junction, *Phys. Rev. B* **83**, 195441 (2011).
 - [2] J.-X. Zhang and C.-X. Liu, Disordered quantum transport in quantum anomalous hall insulator-superconductor junctions, *Phys. Rev. B* **102**, 144513 (2020).
 - [3] M. P. A. Fisher, Cooper-pair tunneling into a quantum hall fluid, *Phys. Rev. B* **49**, 14550 (1994).
 - [4] B. Béri, J. N. Kupferschmidt, C. W. J. Beenakker, and P. W. Brouwer, Quantum limit of the triplet proximity effect in half-metal-superconductor junctions, *Phys. Rev. B* **79**, 024517 (2009).
 - [5] O. Entin-Wohlman, Y. Imry, and A. Aharony, Conductance of superconducting-normal hybrid structures, *Phys. Rev. B* **78**, 224510 (2008).
 - [6] T. H. Galambos, F. Ronetti, B. Hetényi, D. Loss, and J. Klinovaja, Crossed andreev reflection in spin-polarized chiral edge states due to the meissner effect, *Phys. Rev. B* **106**, 075410 (2022).
 - [7] Y. Tang, C. Knapp, and J. Alicea, Vortex-enabled andreev processes in quantum hall-superconductor hybrids, *Phys. Rev. B* **106**, 245411 (2022).
 - [8] V. D. Kurilovich and L. I. Glazman, Criticality in the crossed andreev reflection of a quantum hall edge, *Phys. Rev. X* **13**, 031027 (2023).
 - [9] N. Schiller, B. A. Katzir, A. Stern, E. Berg, N. H. Lindner, and Y. Oreg, Superconductivity and fermionic dissipation in quantum hall edges, *Phys. Rev. B* **107**, L161105 (2023).
 - [10] K. V. Mardia and P. E. Jupp, eds., *Directional Statistics*, Wiley Series in Probability and Statistics (J. Wiley, Chichester New York, 2010).
 - [11] Y. Kawada and K. Itô, On the probability distribution on a compact group. i, Proceedings of the Physico-Mathematical Society of Japan. 3rd Series **22**, 977 (1940).
 - [12] B. Lian, J. Wang, X.-Q. Sun, A. Vaezi, and S.-C. Zhang, Quantum phase transition of chiral majorana fermions in the presence of disorder, *Phys. Rev. B* **97**, 125408 (2018).

- [13] M. Buttiker, Symmetry of electrical conduction, *IBM J. Res. Dev.* **32**, 317 (1988).
- [14] G. Cui, X. Yu, S. Iommelli, and L. Kong, Exact distribution for the product of two correlated gaussian random variables, *IEEE Signal Process. Lett.* **23**, 1662 (2016).
- [15] Y. Hu, J. Wang, and B. Lian, Resistance distribution of decoherent quantum hall-superconductor edges (2024), [arXiv:2405.17550](https://arxiv.org/abs/2405.17550) [cond-mat].
- [16] C.-Z. Chang, J. Zhang, X. Feng, J. Shen, Z. Zhang, M. Guo, K. Li, Y. Ou, P. Wei, L.-L. Wang, Z.-Q. Ji, Y. Feng, S. Ji, X. Chen, J. Jia, X. Dai, Z. Fang, S.-C. Zhang, K. He, Y. Wang, L. Lu, X.-C. Ma, and Q.-K. Xue, Experimental observation of the quantum anomalous hall effect in a magnetic topological insulator, *Science* **340**, 167 (2013).
- [17] D. Zhang, M. Shi, T. Zhu, D. Xing, H. Zhang, and J. Wang, Topological axion states in the magnetic insulator MnBi_2Te_4 with the quantized magnetoelectric effect, *Phys. Rev. Lett.* **122**, 206401 (2019).
- [18] J. Wang, Q. Zhou, B. Lian, and S.-C. Zhang, Chiral topological superconductor and half-integer conductance plateau from quantum anomalous hall plateau transition, *Phys. Rev. B* **92**, 064520 (2015).
- [19] D. J. Thouless and S. Kirkpatrick, Conductivity of the disordered linear chain, *J. Phys. C: Solid State Phys.* **14**, 235 (1981).
- [20] M. P. L. Sancho, J. M. L. Sancho, and J. Rubio, Quick iterative scheme for the calculation of transfer matrices: Application to mo (100), *J. Phys. F: Met. Phys.* **14**, 1205 (1984).
- [21] M. P. L. Sancho, J. M. L. Sancho, J. M. L. Sancho, and J. Rubio, Highly convergent schemes for the calculation of bulk and surface green functions, *J. Phys. F: Met. Phys.* **15**, 851 (1985).
- [22] A. MacKinnon, The calculation of transport properties and density of states of disordered solids, *Z. Physik B: Condens. Matter* **59**, 385 (1985).
- [23] S. Datta, *Lessons from Nanoelectronics: A New Perspective on Transport*, second edition ed., Lessons from Nanoscience: A Lecture Notes Series No. vol. 5 (World Scientific, New Jersey, 2017).
- [24] Q.-f. Sun and X. C. Xie, Quantum transport through a graphene nanoribbon–superconductor junction, *J. Phys.: Condens. Matter* **21**, 344204 (2009).
- [25] B. Lian, J. Wang, and S.-C. Zhang, Edge-state-induced andreev oscillation in quantum anomalous hall insulator-superconductor junctions, *Phys. Rev. B* **93**, 161401 (2016).